International Journal of Greenhouse Gas Control 113 (2022) 103552

Contents lists available at ScienceDirect

International Journal of Greenhouse Gas Control

journal homepage: www.elsevier.com/locate/ijggc

CO_2 Storage in deep saline aquifers: impacts of fractures on hydrodynamic trapping

Yuhang Wang [*,a,b], Cornelis Vuik [a], Hadi Hajibeygi [b]

[a] Faculty of Electrical Engineering, Mathematics and Computer Science, Department of Applied Mathematics, Delft University of Technology, Van Mourik Broekmanweg 6, Delft 2628 XE, the Netherlands

[b] Faculty of Civil Engineering and Geosciences, Department of Geoscience and Engineering, Delft University of Technology, Stevinweg 1, Delft, 2628CV, the Netherlands

ARTICLE INFO

Keywords:
Geologic carbon storage
Multiphase flow in porous media
Embedded discrete fracture model
Compositional simulation

ABSTRACT

Natural or induced fractures are typically present in subsurface geological formations. Therefore, they need to be carefully studied for reliable estimation of the long-term carbon dioxide storage. Instinctively, flow-conductive fractures may undermine storage security as they increase the risk of CO_2 leakage if they intersect the CO_2 plume. In addition, fractures may act as flow barriers, causing significant pressure gradients over relatively small regions near fractures. Nevertheless, despite their high sensitivities, the impact of fractures on the full-cycle storage process has not been fully quantified and understood. In this study, a numerical model is developed and applied to analyze the role of discrete fractures on the flow and transport mechanism of CO_2 plumes in simple and complex fracture geometries. A unified framework is developed to model the essential hydro-geological trapping mechanisms. Importantly, the projection-based embedded discrete fracture model is incorporated into the framework to describe fractures with varying conductivities. Impacts of fracture location, inclination angle, and fracture-matrix permeability ratio are systemically studied for a single fracture system. Moreover, the interplay between viscous and gravity forces in such fractured systems is analyzed. Results indicate that the fracture exhibits differing effects regarding different trapping mechanisms. Generally speaking, highly-conductive fractures facilitate dissolution trapping while weakening residual trapping, and flow barriers can assist dissolution trapping for systems with a relatively low gravity number. The findings from the test cases for single fracture geometries are found applicable to a larger-scale domain with complex fracture networks. This indicates the scalability of the study for field-relevant applications.

1. Introduction

Carbon dioxide capture and storage is essential to mitigate climate change and global warming. Subsurface geological media provide many opportunities for a long-term secure storage (Eiken et al., 2011). Candidate formations include depleted hydrocarbon fields, saline aquifers and unmineable coal seams. Among them, saline aquifers provide the biggest volumetric storage capacities (Bachu, 2002). Injected CO_2 can be trapped in saline aquifers through different trapping mechanisms, including structural or stratigraphic trapping, residual trapping, dissolution trapping, and mineral trapping (Benson and Cole, 2008). These trapping mechanisms operate at varying time scales of dominance. Structural (also referred to as "stratigraphic") trapping occurs as soon as the injected CO_2 migrates towards the top of the aquifer due to the buoyancy forces, and residual trapping takes place at the trailing edge of CO_2 plume mainly after injection ceases (Ide et al., 2007; Juanes et al., 2006). Both of them take effect in relatively early stages of the operation time. In contrast, the dissolution and mineral trapping mechanisms span much longer time periods. Dissolution trapping occurs as early as (usually super-critical) CO_2 contacts the residing undersaturated reservoir brine. The brine charged with dissolved CO_2 molecules becomes denser. This triggers the density-driven convection in post-injection period (Emami-Meybodi et al., 2015; Neufeld et al., 2010; Soltanian et al., 2016). In the meantime, dissolved CO_2 combined with H_2O forms carbonic acid, which induces the dissolution/precipitation of minerals in the rock (Dai et al., 2020). Since saline aquifers often reside in sandstone formations, in which the principle mineral is quartz, geochemical reactions contributed to mineral trapping are insignificant

* Corresponding author at: Faculty of Electrical Engineering, Mathematics and Computer Science, Department of Applied Mathematics, Delft University of Technology, Van Mourik Broekmanweg 6, 2628 XE Delft, the Netherlands.

E-mail addresses: Y.Wang-25@tudelft.nl (Y. Wang), c.vuik@tudelft.nl (C. Vuik), h.hajibeygi@tudelft.nl (H. Hajibeygi).

https://doi.org/10.1016/j.ijggc.2021.103552
Received 20 July 2021; Received in revised form 1 November 2021; Accepted 7 December 2021
Available online 18 December 2021

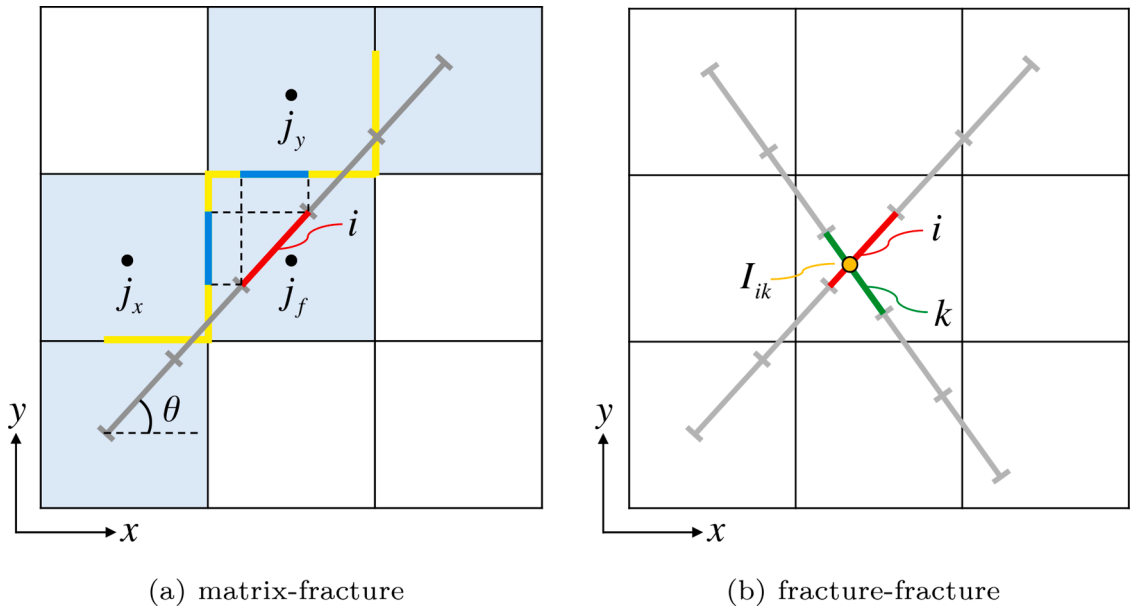

Fig. 1. Schematic of flux calculations between matrix-fracture and fracture-fracture connections. (a): Matrix cells in blue are connected to the fracture segment directly. The continuous projection path of the fracture segment is depicted by a polyline in yellow. A fracture cell *i*, highlighted in red, is used to illustrate the calculation of transmissibility between non-neighboring matrix-fracture connections in pEDFM. (b): Two fracture cells *i* and *k*, highlighted in red and green, from two fracture segments are intersected at I_{ik}. (For interpretation of the references to colour in this figure legend, the reader is referred to the web version of this article.)

(Gunter et al., 2000). As such, in this work, we will focus on the first three trapping mechanisms: i.e., structural, residual and dissolution trapping; referred to as "hydrodynamic" mechanisms (Bachu et al., 1994).

Fractures are observed in pilot and demonstration-scale storage sites (Iding and Ringrose, 2010; Kim et al., 2018). Additionally, hydraulic fracturing has been also applied to increase the injected CO_2 volume (Lucier and Zoback, 2008; Raziperchikolaee et al., 2013). Both natural or artificially-induced fractures, typically, have small apertures sizes on the order of millimeters and below. Despite their narrow apertures, they have significant impacts on flow patterns, due to the large contrast between their permeability (flowing conductivity) and the hosting reservoir rock. Therefore, high fidelity representation of these geological features by explicitly representing them in the computational grids is required for accurate numerical simulations Berkowitz (2002). The class of methods developed to explicitly capture fractures are referred to as discrete fracture modeling (DFM) approaches (Berre et al., 2019).

There exist two main classes of DFM: (1) the conforming approach using unstructured grids (U-DFM) and (2) the non-conforming method with structured mesh. In U-DFM model, fractures are treated as constraints lying along the interfaces of the matrix grid cells (Ahmed et al., 2015; Jiang and Younis, 2015; Karimi-Fard et al., 2004; Reichenberger et al., 2006). As such an unstructured mesh is essential as it offers flexibility to allow grid cells conforming to geometric constraints. To capture the transient behavior of flow, local grid refinement is often applied in the vicinity of fractures (Hui et al., 2018; Karimi-Fard and Durlofsky, 2016; Mustapha et al., 2011; Sun et al., 2016; Wang and Shahvali, 2016). Note that in U-DFM, accurate representation of fracture geometry requires a relatively large number of grids with potentially complex geometries, which lead to significant computational costs when modeling field-scale reservoirs. On the other hand, non-conforming methods were proposed to deal with fractured systems. Specifically, even structured grids can be used to represent the rock matrix, while each fracture is represented by an independent suited grid. Prominent examples include (a) the embedded discrete fracture modeling (EDFM), and (b) the extended finite element method (XFEM). In EDFM, the flux exchange between a matrix cell and its embedded fracture is expressed with the same analogy as in the discrete form of Darcy's law (Hajibeygi et al., 2011; Lee et al., 2000; Li and Lee, 2008). It has been applied to describe reservoirs containing highly-conductive fractures (Moinfar et al., 2014; Norbeck et al., 2016; Xu et al., 2017), or used as an upscaling approach to compute effective transmissibility (Fumagalli et al., 2016; 2017). In addition, EDFM can be coupled with multiscale methods to improve the efficiency of flow simulation (Ţene et al., 2016). XFEM, on the other hand, extends the classical finite element method by adding discontinuous basis functions to capture discontinuity in the solution space (Moës et al., 1999; Xu et al., 2021). This method is originally developed to model cracks and crack growth for fracture mechanics, and it has been applied to simulating flow in fractured porous media (Flemisch et al., 2016).

Comprehensive benchmarking studies between U-DFM, EDFM, and XFEM have been conducted in the literature (Berre et al., 2021; Flemisch et al., 2018), where EDFM was shown to fail capturing poorly-conductive flow-barrier fractures, i.e., fractures with permeability lower than that of the matrix. This is not surprising as EDFM does not alter the connectivities between the neighboring matrix cells, irrespective of the embedded fracture elements. To overcome this major limitation, Ţene et al. (2017) proposed a new formulation named the projection-based EDFM (pEDFM). The proposed model adjusts the matrix-matrix and matrix-fracture transmissibilities such that effects of fractures are consistently represented in the computational mesh. pEDFM outperforms EDFM, specially when fractures are barriers to flow.

Fractured reservoirs are in general assumed to be inappropriate for secure long-term CO_2 storage, because highly conductive fractures produce preferential pathways which may lead to potential leakage through faults and abandoned wells (Bruant et al., 2002; Dockrill and Shipton, 2010; Zhang et al., 2018). Moreover, injection operations increase pore pressure and may reactivate faults, increasing risks of seismicity. Careful evaluation of fault responses with respect to pore pressure fluctuations is therefore essential in determining appropriate injection schemes (Espinoza and Santamarina, 2017; Rinaldi et al., 2014; Rutqvist, 2012; Zappone et al., 2021), which is out of the scope of this work. Efforts have been made to investigate CO_2 plume migration during injection period in a fractured system (Ahmed and Li, 2019; Ren et al., 2017). However, these studies are mainly focused on the

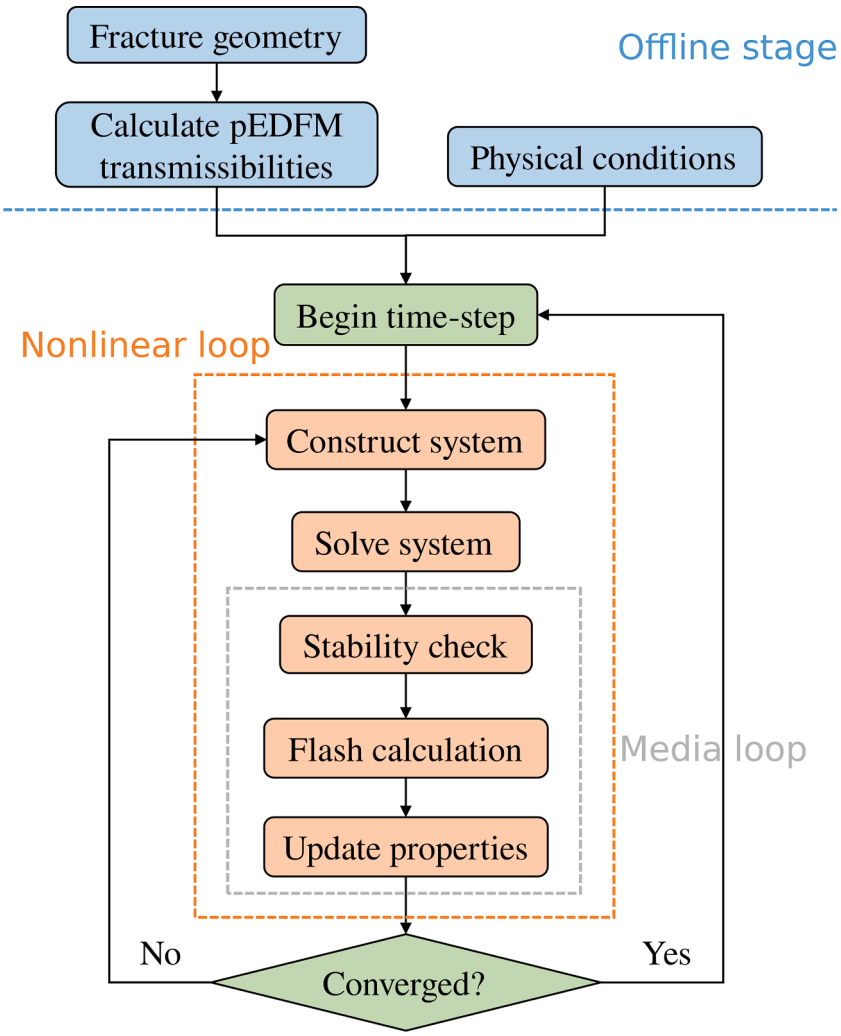

Fig. 2. Workflow of the compositional framework for fractured systems.

development of discretization schemes; and leave the important underlying physics associated with hydrodynamic trapping mechanisms either simplified or ignored. As for the post-injection period, the role of fractures in density-driven convection has recently received increased attention (Kim et al., 2019; Shafabakhsh et al., 2021). In these analyses, the initial conditions are set such that a dissolved/saturated layer exists on top of the domain, and a perturbation is imposed on the layer to trigger flow instability. More precisely, these studies neglect the velocity and saturation fields created by advective transport during the injection period. In addition, most of previous work treat fractures as highly-conductive flow pathways, and only few discussed scenarios in which the fracture permeability is lower than that of the matrix. The target formation may nevertheless contain fractures with a wide range of conductivities. Of great importance is to develop a robust modeling strategy for both barrier and highly-conductive fractures, and to assess the full-cycle dynamics of trapping, from the beginning of the operation injection to the post migration phase. Such a study would reveal important insights as to what roles fractures of different conductivities play in the mechanisms of residual and dissolution trapping.

This work presents the development of a robust modeling approach and quantification of the role of fractures in CO_2 storage mechanisms. Fractures are explicitly represented by pEDFM, allowing for the studying of the impact of fractures with varying permeability contrasts. We consider hysteretic experimental-based constitutive relations in order to represent the real-field process scenarios. The development is built on a unified framework of a compositional formulation to describe the relevant physics of the CO_2-brine system. The model is solved with a fully-implicit, fully-coupled strategy to assess the full-cycle CO_2 evolution in saline aquifers. Our study does not assume time-scale separation between the acting mechanisms, but allows for investigation of the scale of each mechanism along the entire simulation time. To the best of our knowledge, such a study is unique in the literature, and provides a significant step forward in the quantification of the storage in complex fractured geological media.

The paper is structured as follows. First, we briefly revisit the governing equations and physical models used to capture the hydrodynamic trapping. Then we apply this numerical model to an illustrative domain with a single fracture of different configurations. We evaluate the impacts of fracture location, inclination angle, and conductivity on the time-lapsed behavior of residual and dissolution trapping for a full-cycle storage process. We also study the interplay of viscous and gravity forces in such fractured systems by adjusting the gravity number, defined as the ratio of gravity to viscous forces. Next, we simulate such process in a complex fracture network which is representative of field-scale fractured system. Finally, we close with conclusions and possible directions for future work.

2. Physical models and methods

2.1. Governing equations

Fluids are described using a two-phase, two-component system. In

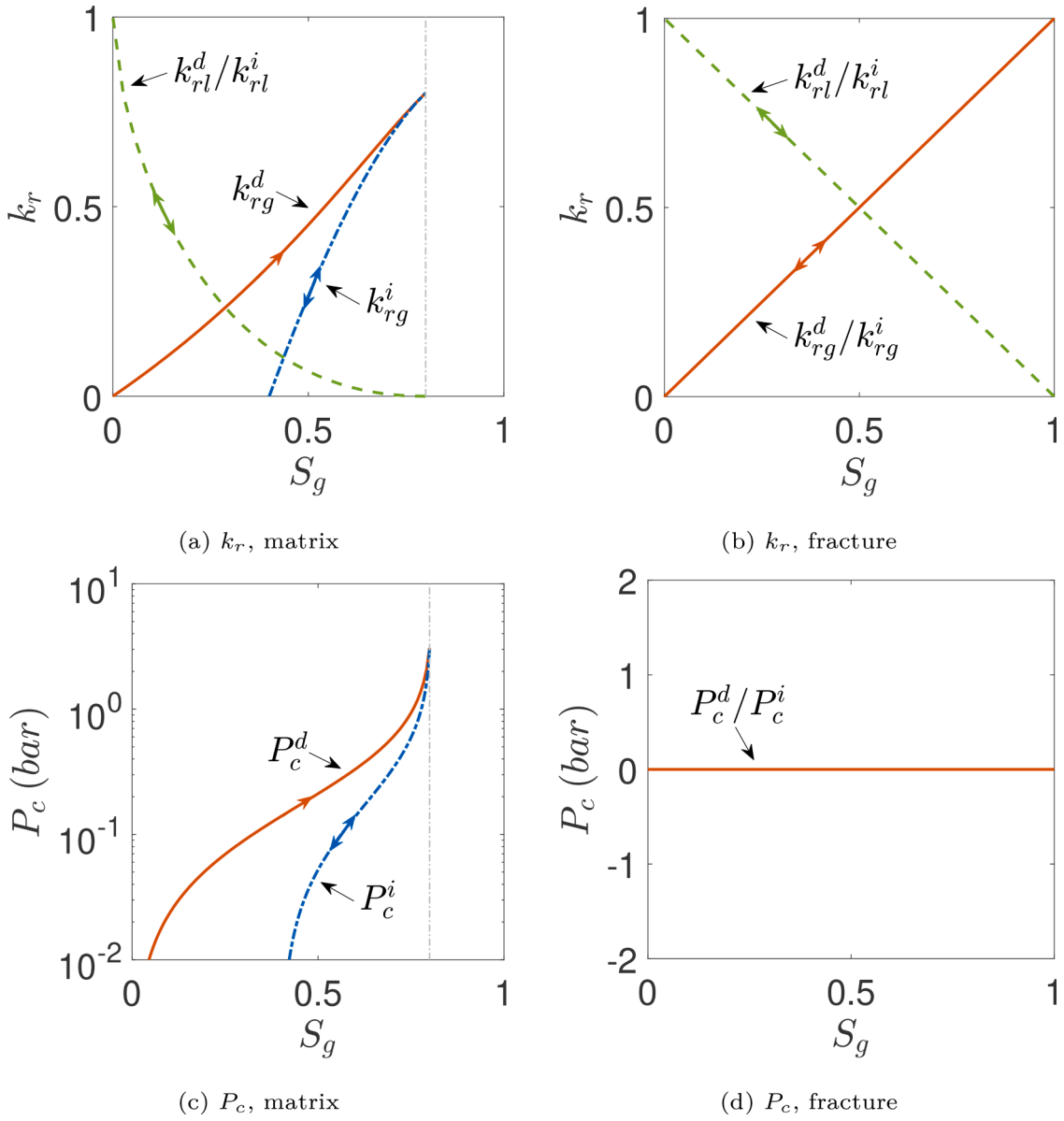

Fig. 3. Illustration of constitutive relations used for the matrix and fractures. The superscript *d* and *i* denote drainage and imbibition, respectively. Single/Double headed arrow indicates that the process along a given curve is irreversible/reversible, respectively.

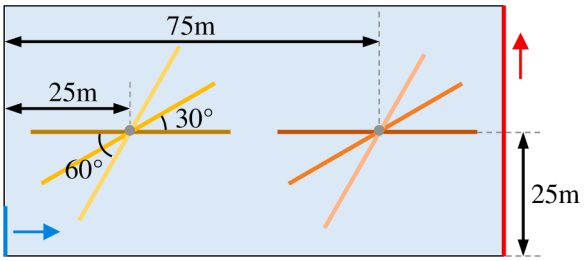

Fig. 4. Schematic of 100 × 50m computational domain and fracture geometries for cases of single fracture.

particular, gas and liquid phases are presented, which are composed of two components, CO_2 and brine. We consider that CO_2 exists in both phases whereas brine exists in the liquid phase only. The generalized mass conservation equations for matrix and fractures are, respectively, expressed as

Table 1
Physical parameters and simulation settings for the cases of single fracture media. (ppm: parts per million; PV: pore volume.)

Parameter	Value	Unit
Aquifer length	100	m
Aquifer height	50	m
Fracture length	40	m
Fracture aperture	5.0e-3	m
Fracture inclination angle	0/30/60	°
Matrix porosity	0.2	-
Matrix permeability	8.0e-14/4.0e-15	m^2
Initial pressure	2.5e7	Pa
Bottom hole pressure	2.5e7	Pa
Temperature	338.15	K
CO_2 density at STC	1.98	kg/m^3
Brine salinity	1.0e5	ppm
Brine density at STC	1060	kg/m^3
Injection rate	6.5e-5	PV/day
Simulation time	3.6e4	day
Injection time	6.0e2	day

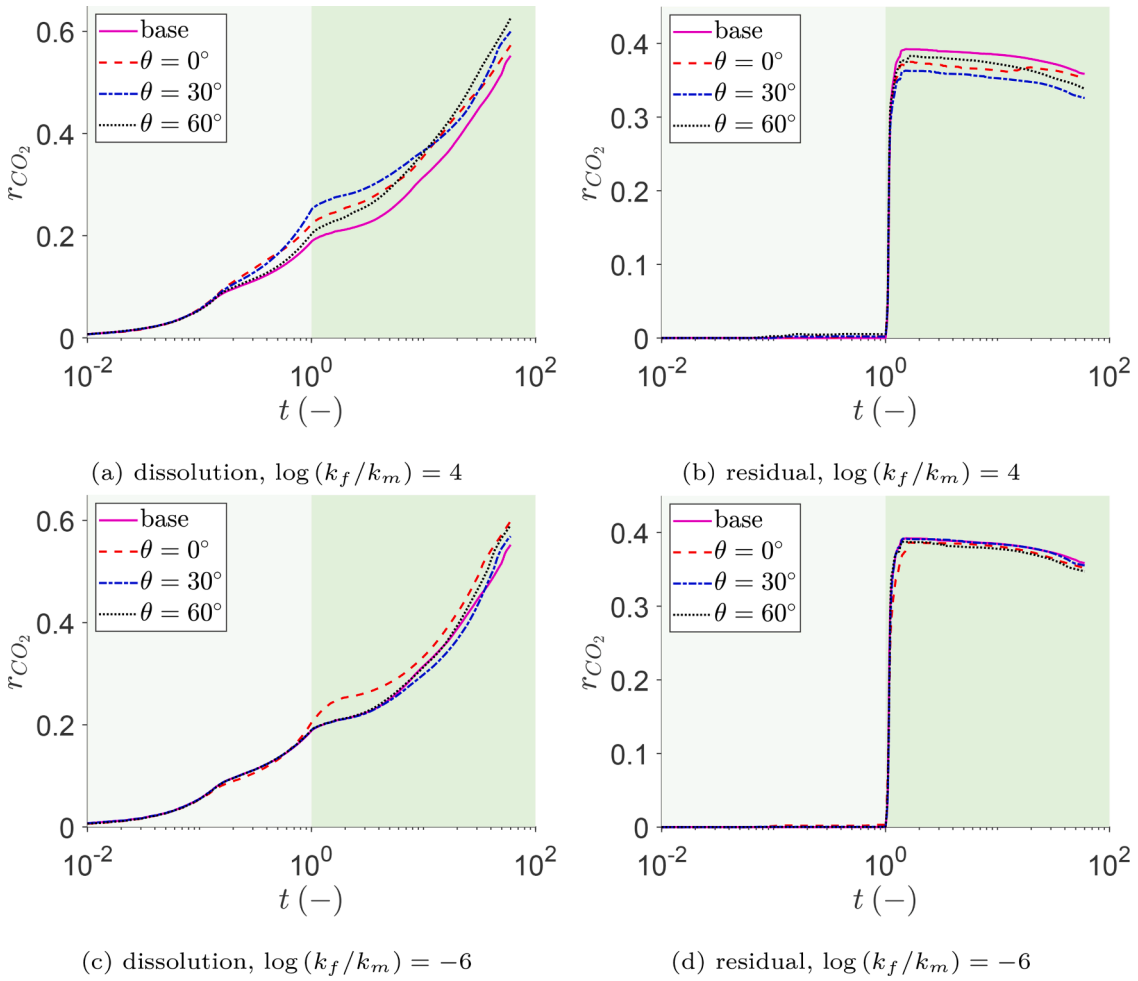

Fig. 5. Fraction of injected CO_2 trapped by different mechanisms in cases of a fracture placed near the injection well ($k_m = 8.0 \times 10^{-14}$ m^2).

$$\frac{\partial}{\partial t}\left(\phi^m \sum_\alpha x_{c,\alpha}\rho_\alpha S_\alpha\right) + \nabla\cdot\left(\sum_\alpha x_{c,\alpha}\rho_\alpha \boldsymbol{u}_\alpha\right) - \sum_\alpha x_{c,\alpha} q_\alpha - \sum_\alpha x_{c,\alpha} Q_\alpha^{mf} = 0, \tag{2.1}$$

and

$$\frac{\partial}{\partial t}\left(\phi^f \sum_\alpha x_{c,\alpha}\rho_\alpha S_\alpha\right) + \nabla\cdot\left(\sum_\alpha x_{c,\alpha}\rho_\alpha \boldsymbol{u}_\alpha\right) - \sum_\alpha x_{c,\alpha} Q_\alpha^{fm} - \sum_\alpha x_{c,\alpha} Q_\alpha^{ff} = 0, \tag{2.2}$$

where superscripts m and f denote matrix and fracture, respectively; subscripts α and c denote phases (gas and liquid) and components (CO_2 and brine). Moreover, ϕ is porosity, ρ_α and S_α are the density and saturation of phase α. $x_{c,\alpha}$ is the mole (mass) fraction of component c in phase α; q_α is the sources term, e.g. injection/production wells, associated with matrix; Q^{mf} and Q^{fm} are fluxes between matrix and fractures, and Q^{ff} is flux between intersecting fractures. These matrix-fracture and fracture-fracture coupling terms are computed based on the associated transmissibilities, i.e., T^{mf} and T^{ff}, using pEDFM (Ţene et al., 2017; HosseiniMehr et al., 2018). Darcy velocity $\boldsymbol{u}_\alpha$ is given by

$$u_\alpha = -\frac{k k_{r\alpha}}{\mu_\alpha}\nabla\psi_\alpha, \tag{2.3}$$

where k is rock permeability, $k_{r\alpha}$, μ_α, and ψ_α are the relative permeability, viscosity, and potential of phase α.

To illustrate the calculation of flux terms (Q^{mf} and Q^{ff}), two schematics are depicted Fig. 1. As shown in Fig. 1a, a fracture segment intersects matrix cells on a discrete domain. The continuous projection path of this fracture segment is represented by a polyline in yellow along the edges of matrix cells. Consider the fracture cell i (in red) embedded in the matrix cell j_f. The associated projection of cell i along each dimension, i.e., x- and y-axis in this case, is highlighted in blue on the projection path. The matrix cell j_f is connected to the fracture cell i directly, meanwhile matrix cells j_x and j_y are also connected to the fracture cell i as non-neighboring connections. The flux between fracture cell i and matrix cell j ($j \in \{j_f, j_x, j_y\}$) of phase α, Q_α^{ij}, is given by

$$Q_\alpha^{ij} = \left(\rho_\alpha \frac{k_{r\alpha}}{\mu_\alpha}\right)^* T^{ij}\Delta\psi_\alpha^{ij} \tag{2.4}$$

in a general manner, where the superscript $*$ denotes that the property is evaluated using the phase potential upwind scheme. T^{ij} is the geometrical transmissibility given by

$$T^{ij} = k^{ij} CI^{ij}, \tag{2.5}$$

where k^{ij} is the harmonically-averaged permeability, and CI_{ij} is the connectivity index given by

$$CI^{ij} = \frac{A^{ij}}{\langle d\rangle^{ij}}, \tag{2.6}$$

where $\langle d\rangle^{ij}$ is the average distance between these two cells. For $j = j_f$, A^{ij_f} is the area of intersection between fracture cell i and matrix cell j_f. A^{ij_x} and A^{ij_y} are the projection areas of A^{ij_f} given by

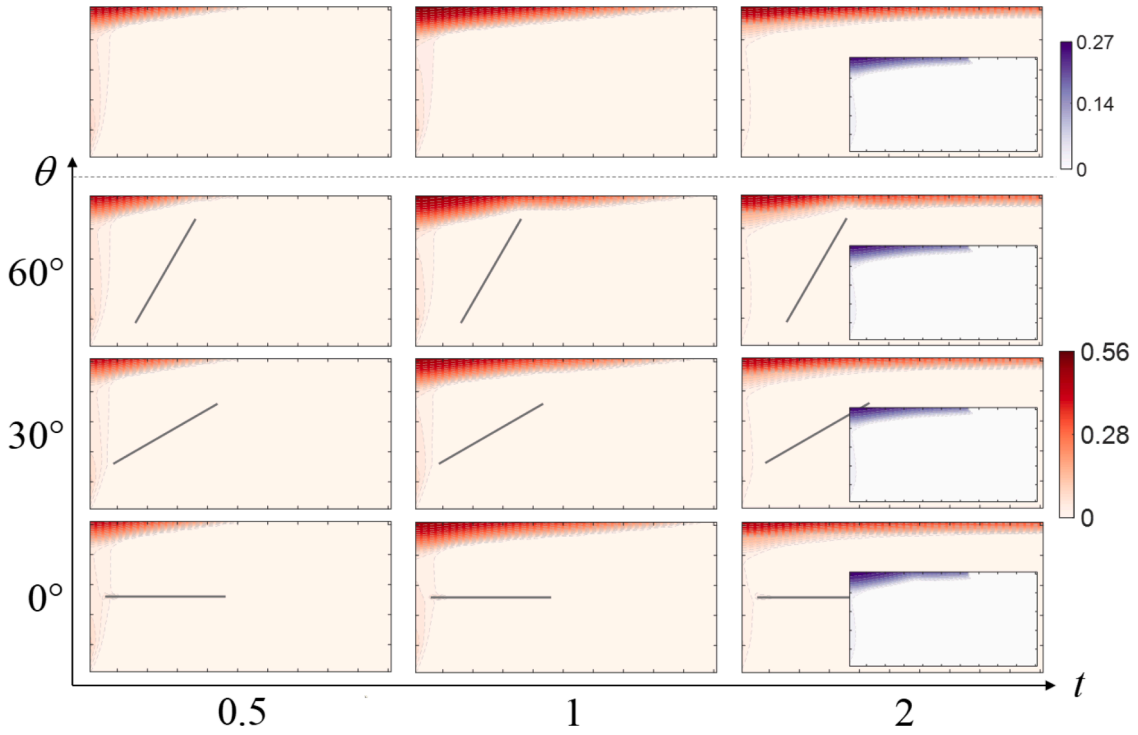

Fig. 6. Saturation maps of the gas phase in cases of a highly-conductive fracture placed near the injection well ($k_m = 8.0 \times 10^{-14}$ m^2). Results obtained from the base case (without fractures) are presented on top. Residual saturation profiles at $t = 2$ are embedded in associated saturation maps.

$$A^{ij_x} = A^{ij_f} \sin\theta, \text{ and } A^{ij_y} = A^{ij_f} \cos\theta, \tag{2.7}$$

where θ is the inclination angle of the fracture segment.

The flux between two intersecting fracture cells i and k (shown in Fig. 1b) of phase α is expressed as

$$Q_\alpha^{ik} = \left(\rho_\alpha \frac{k_{r\alpha}}{\mu_\alpha}\right)^* T^{ik} \Delta\psi_\alpha^{ik}, \tag{2.8}$$

where

$$T^{ik} = k^{ik} \frac{CI^{il_{ik}} CI^{kl_{ik}}}{CI^{il_{ik}} + CI^{kl_{ik}}}. \tag{2.9}$$

In this equation, $CI^{il_{ik}}$ and $CI^{kl_{ik}}$ denote the connectivity indexes between the fracture cells and the intersection point I_{ik}.

The overall-composition variable set is used (Voskov and Tchelepi, 2012), in which the liquid phase pressure, p_l, and CO_2 mole (mass) fraction, z_{CO_2}, are used as primary variables (Cusini et al., 2018). The residuals are linearized with respect to primary variables given by

$$r_c^{\nu+1} \approx r_c^{\nu} + \frac{\partial r_c}{\partial p_l}\bigg|^{\nu} \delta p_l^{\nu+1} + \frac{\partial r_c}{\partial z_{CO_2}}\bigg|^{\nu} \delta z_{CO_2}^{\nu+1} = 0, \tag{2.10}$$

where ν and $\nu+1$ are iteration steps. In each iteration step the linear system to be solved is expressed as

$$\begin{pmatrix} \frac{\partial r_b^m}{\partial p_l^m} & \frac{\partial r_b^m}{\partial p_l^f} & \frac{\partial r_b^m}{\partial z_{CO_2}^m} & \frac{\partial r_b^m}{\partial z_{CO_2}^f} \\ \frac{\partial r_b^f}{\partial p_l^m} & \frac{\partial r_b^f}{\partial p_l^f} & \frac{\partial r_b^f}{\partial z_{CO_2}^m} & \frac{\partial r_b^f}{\partial z_{CO_2}^f} \\ \frac{\partial r_{CO_2}^m}{\partial p_l^m} & \frac{\partial r_{CO_2}^m}{\partial p_l^f} & \frac{\partial r_{CO_2}^m}{\partial z_{CO_2}^m} & \frac{\partial r_{CO_2}^m}{\partial z_{CO_2}^f} \\ \frac{\partial r_{CO_2}^f}{\partial p_l^m} & \frac{\partial r_{CO_2}^f}{\partial p_l^f} & \frac{\partial r_{CO_2}^f}{\partial z_{CO_2}^m} & \frac{\partial r_{CO_2}^f}{\partial z_{CO_2}^f} \end{pmatrix} \begin{pmatrix} \delta p_l^m \\ \delta p_l^f \\ \delta z_{CO_2}^m \\ \delta z_{CO_2}^f \end{pmatrix} = - \begin{pmatrix} r_b^m \\ r_b^f \\ r_{CO_2}^m \\ r_{CO_2}^f \end{pmatrix}. \tag{2.11}$$

Here the subscript 'b' is short for brine. This system is solved using a fully-implicit scheme (Aziz, 1979). Fig. 2 shows the overall workflow of the developed computational platform. Computation of pEDFM transmissibilities (T^{mf} and T^{ff}) is performed based on the predefined fracture geometry in the offline stage. In the nonlinear loop, a stability check and flash calculation are conducted after solving the linearized system, followed by an update of the relevant physical properties. These steps, referred to as the "Media loop" in Fig. 2 are sequentially performed for the fracture and matrix media.

2.2. Physical models

In hydrodynamic trapping mechanisms, the structural trapping is modeled by no-flow boundary conditions imposed on top of the computational domain. The other two, i.e., dissolution and residual ones, are incorporated in descriptions of fluid properties and constitutive relations, respectively. Dissolution trapping is considered in the model via the solution CO_2-brine ratio, R_s, which is defined as

$$R_s = \frac{V_{CO_2}^{STC}}{V_b^{STC}}, \tag{2.12}$$

where $V_{CO_2}^{STC}$ and V_b^{STC} are volumes of dissolved CO_2 and the associated formation brine at standard conditions (denoted by superscript 'STC'), respectively. R_s is calculated based on properties of a CO_2-brine mixture at equilibrium state given by Hassanzadeh et al. (2008)

$$R_s = \frac{\rho_b^{STC} x_{CO_2,l}}{\rho_{CO_2}^{STC}\left(1 - x_{CO_2,l}\right)}. \tag{2.13}$$

Here properties of the mixture at equilibrium state are computed following the thermodynamic model based on equating chemical potentials (Spycher et al., 2003). The calculated CO_2-brine ratio as a function of pressure is translated into look-up tables in the simulation. R_s is related to liquid phase density given by

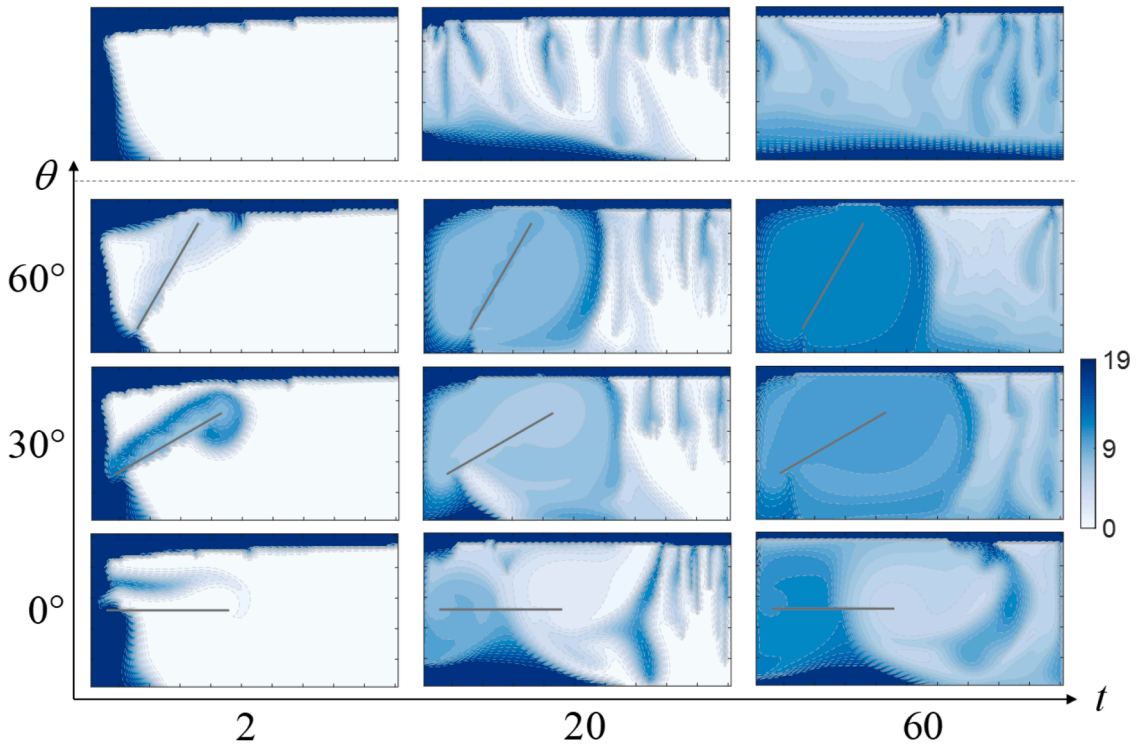

(a) $\log(k_f/k_m) = 4$

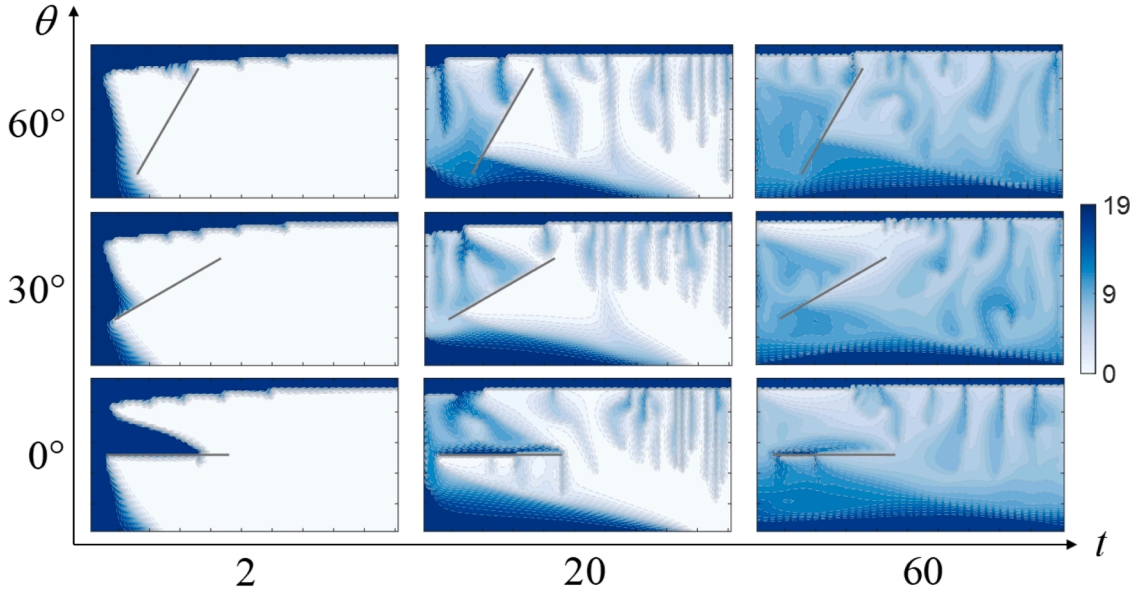

(b) $\log(k_f/k_m) = -6$

Fig. 7. Solution CO_2-brine ratio profiles in cases of a fracture placed near the injection well ($k_m = 8.0 \times 10^{-14}$ m^2). Results obtained from the base case (without fractures) are presented on top of the cases with $\log(k_f/k_m) = 4$.

$$\rho_l = \frac{\rho_b^{STC} + \rho_{CO_2}^{STC} R_s}{B_b}, \tag{2.14}$$

where B_b is the formation volume factor of brine. It is worth mentioning that Eq. (2.13) applies to cells in which both phases are present; if the cell is in undersaturated state, i.e., single liquid phase, R_s is calculated by replacing $x_{CO_2,l}$, which appears in Eq. (2.13) with z_{CO_2}.

As for the residual trapping, we propose a robust algorithm to describe the hysteretic behavior of constitutive relations (Wang et al., 2022). In particular, a scanning curve is created to account for the transition of the displacement process (Carlson, 1981; Joekar-Niasar et al., 2013; Killough, 1976; Plohr et al., 2001). Such a curve is obtained based on the primary drainage and imbibition curves, and the associated residual saturation is computed using a linear trapping model (Ni et al., 2019; Ruprecht et al., 2014; Steffy et al., 1997)

$$S_{gr} = f_r S_{gt}, \tag{2.15}$$

where S_{gt} is the saturation at the turning point which the transition occurs, and f_r is a constant fraction. We consider the rock to be strongly

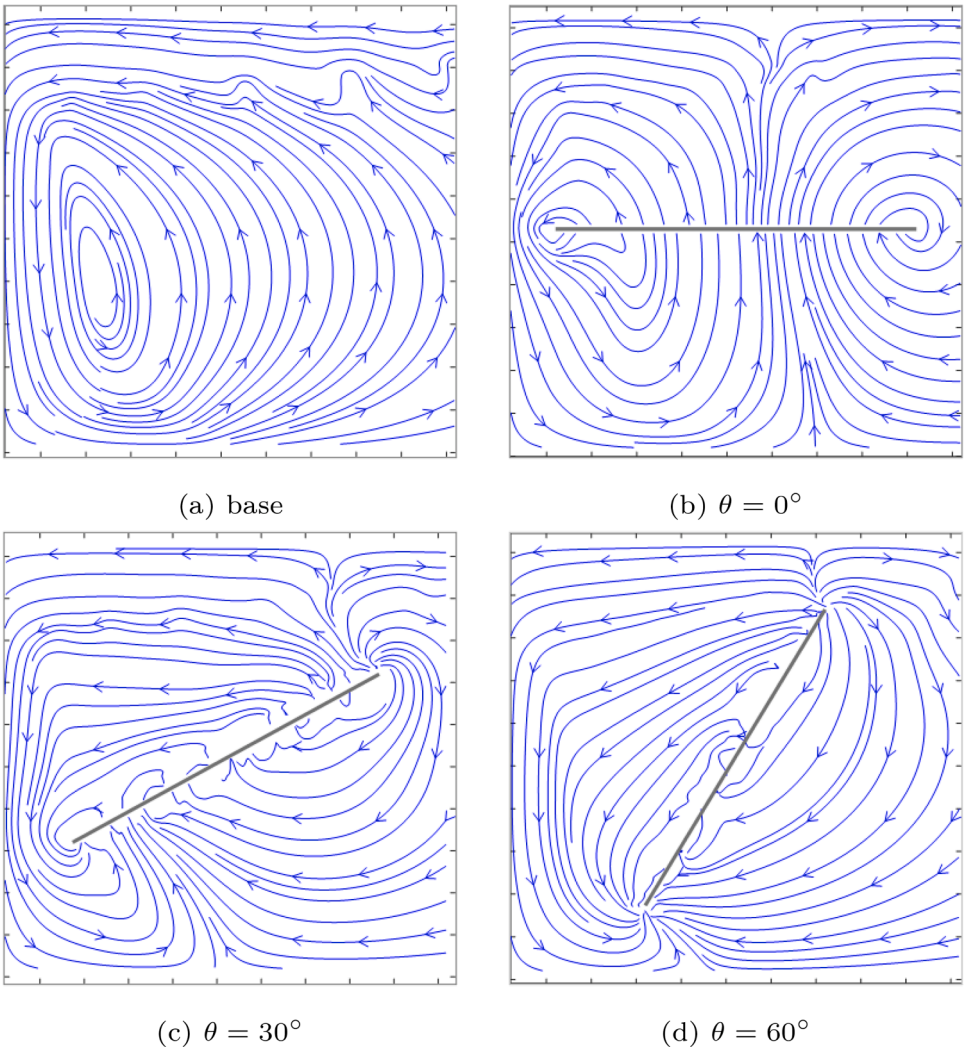

Fig. 8. Streamline distribution of liquid phase in the left half of the aquifer at $t = 2$.

water-wet, therefore, hysteretic behavior is more pronounced in the nonwetting gas phase. Relative permeability curves for matrix are modified from the experimental data reported in literature (Oak et al., 1990) using a van Genuchten equation (van Genuchten, 1980), and capillary pressure curves are given by the Leverett *J*-function. In this work, we assume that the interplay of flow between different phases in the fracture is insignificant. As a result, the relative permeability follows linear curves (Fanchi, 2005). Capillary pressure and hysteresis effects are not considered in fractures. Primary drainage and imbibition curves for matrix and fracture media are presented in Fig. 3.

2.3. Simulation setup

For a systematic investigation of full-cycle CO_2 storage in a fractured saline aquifer, we first consider a two-dimensional, cross section of a saline aquifer with 100m in length and 50m in height. The grid size is 1m in each direction. Such resolution has shown to be sufficient for a converged quantification of the dissolution trapping in our recent study (Wang et al., 2022). An injection well from which CO_2 being injected is set through the bottom 10m of the domain on the left, and a production well penetrating the entire reservoir is set on the right boundary. We place a single fracture in the domain with differing positions and inclination angles - see Fig. 4. Impacts of fracture conductivity are studied by varying the fracture permeability while fixing the fracture aperture. In each scenario, we consider two ratios in logarithmic scale for fracture-matrix permeability, i.e., 4 and -6, which represent highly conductive fractures and flow barriers, respectively. Moreover, the relative significance of viscous forces and gravity forces for such a two-phase system is varied by adjusting the matrix permeability, as indicated by the gravity number defined as (Ide et al., 2007)

$$N_{\mathrm{gv}} = \frac{k_v L \Delta\rho g}{H u \mu_{\mathrm{b}}}, \tag{2.16}$$

where k_v is vertical permeability of matrix, L and H are the aquifer length and height, $\Delta\rho$ is density difference between the liquid and gas phases, g is gravity acceleration constant, and u is the magnitude of characteristic flow velocity. For cases considered in this work, the injection rate is a reasonable indicator of a characteristic velocity. We consider two matrix permeability values, 8.0×10^{-14} m^2 and 4.0×10^{-15} m^2, which correspond to relatively larger/smaller gravity numbers. Physical parameters and simulation settings used in the simulations of single fracture media are summarized in Table 1. Following the systematic investigation we look into a domain of larger scale with complex fracture geometries. The fracture network is generated using a statistical approach. Wells are placed in the same manner as that for the previous case of a single fracture. In the following discussion, the elapsed time (t) is nondimensionalized with respect to the duration of the injection period.

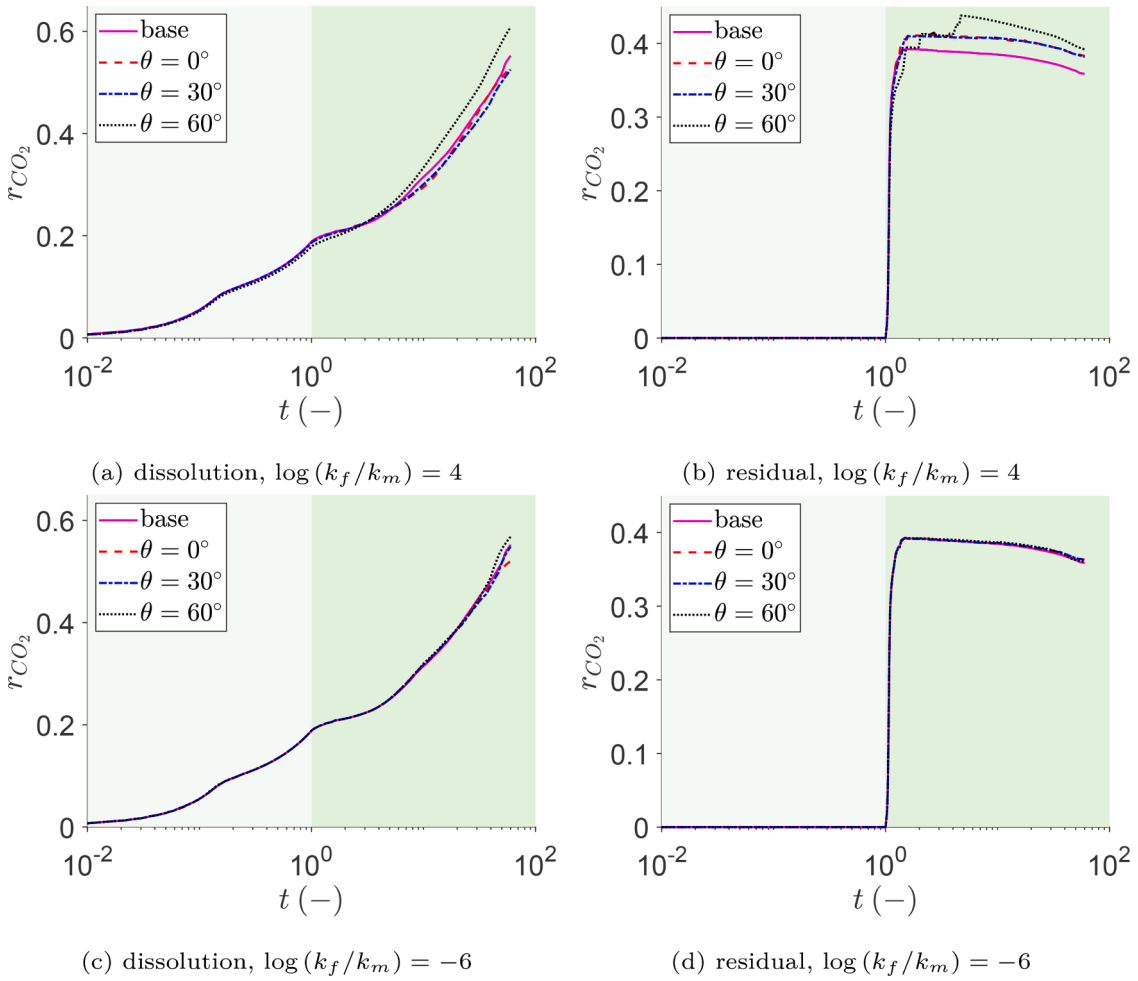

Fig. 9. Fraction of injected CO_2 trapped by different mechanisms in cases of a fracture placed near the production well ($k_m = 8.0 \times 10^{-14}$ m^2).

3. Results and discussions

3.1. Single fracture media (high gravity number)

We first present quantification results for dissolution and residual trapping with the matrix permeability given by $k_m = 8.0 \times 10^{-14}$ m^2. As shown in Fig. 5a, dissolution curves obtained from systems with conductive fractures deviate from that of the base case at an early stage during injection period, whereas differences are insignificant in the presence of flow barriers - see Fig. 5c. This affects residual trapping as shown in Fig. 5b and d. To better understand the impact of dissolution on residual trapping, we present saturation profiles of gas phase at three moments ($t = 0.5$, 1, and 2) close to the cessation of injection shown in Fig. 6. Due to relatively strong gravity forces, CO_2 flows upward immediately after being injected into the aquifer, and forms a gravity tongue underneath the top boundary. Because of such rapid vertical movement, CO_2 flows through the fracture rapidly if the fracture intersects the CO_2 plume, and no CO_2 is accumulated at the fracture tip from which CO_2 exits the fracture and flows back to the aquifer. The residual saturation maps embedded in saturation maps of the gas phase at $t = 2$ indicate that the majority of residual trapping occurs just beneath the top of the aquifer. If more injected gas dissolves into brine during injection, less flows upward which leads to a lower residual saturation. This explains the interaction between residual and dissolution trapping during the injection period.

Time-lapsed behavior of dissolution trapping in the post-injection period is studied via solution CO_2-brine ratio profiles, which depict the flow dynamics of the liquid phase. Fig. 7 shows the solution CO_2-brine ratio maps at three moments in the post-injection period. As seen from Fig. 5a, the simulated case with $\theta = 30°$ has the largest fraction following the cessation of injection. In this case, the fracture is intersected with the CO_2 plume, and in consequence, CO_2 invades the aquifer through this highly conductive fracture and is dissolved along the upper side of the fracture shown in Fig. 7a. We observe that the fracture with $\theta = 0°$ also penetrates the CO_2 plume, however, less CO_2 has dissolved compared to the case with $\theta = 30°$. From here we can infer that in displacements of high N_{gv}, even a highly-conductive fracture may not be sufficient to alter the dominance of gravity forces over viscous forces. At late times ($t = 20$, 60), we observe that the highly-conductive fracture which served as a pathway enhances the circulation of brine over the entire domain.

To examine the development of such enhancement, we depict the streamline distribution of the liquid phase in the left half of the domain at $t = 2$ - see Fig. 8. Fig. 8a presents the result obtained from the base case without fractures. As shown, the saturated brine near the left boundary flows downward driven by the gravity forces, and then streams along the bottom layer before flowing upward following a curved path in this closed system. As such, the liquid phase generates a circulation of flow over the domain. Nevertheless, the presence of the inclined fracture ($\theta = 30°$ and 60°) breaks such circulation by providing a preferential pathway for the upward migration of the liquid phase. A local circulation is formed close to the fracture shown in Fig. 8c and d. As for the horizontal one ($\theta = 0°$), it induces two local circulations with opposite directions. In this case, the fracture does not assist the upward flow of brine, and we observe that the brine with a high concentration of CO_2 accumulates along the bottom boundary (shown in Fig. 7a).

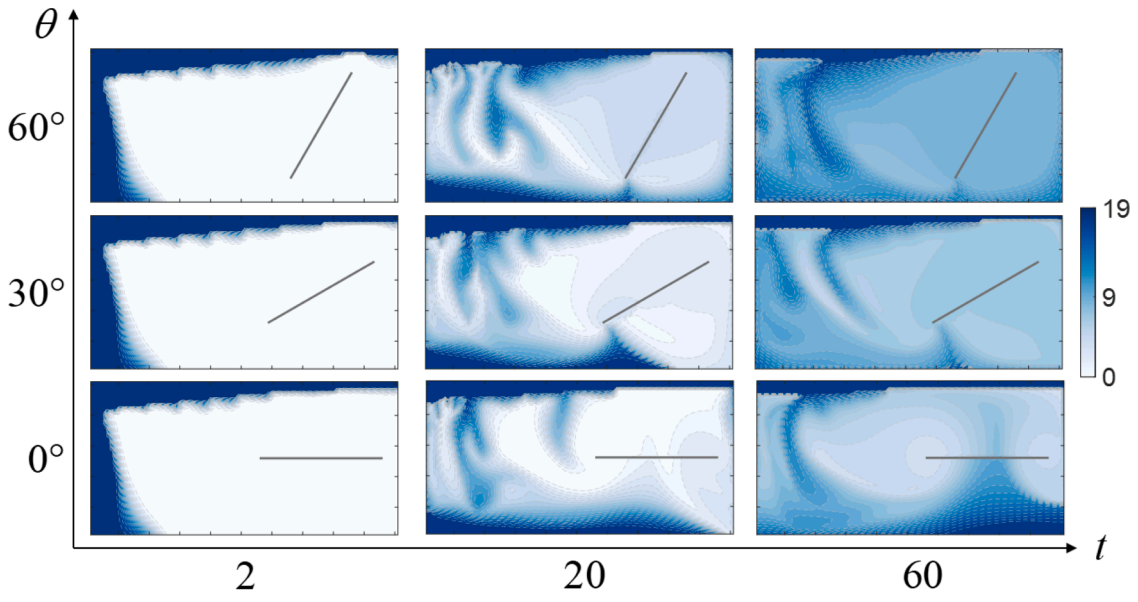

(a) $\log(k_f/k_m) = 4$

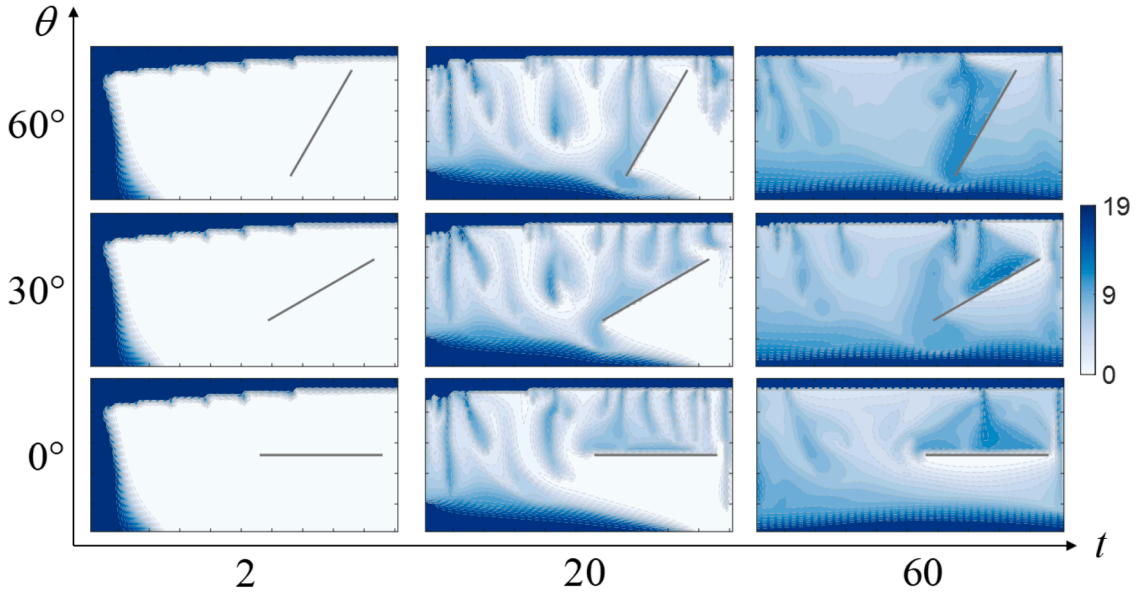

(b) $\log(k_f/k_m) = -6$

Fig. 10. Solution CO_2-brine ratio profiles in cases of a fracture placed near the production well ($k_m = 8.0 \times 10^{-14}$ m^2).

Therefore, the inclined fracture favors dissolution trapping.

On the other hand, when fractures appear as flow barriers, they impede the flow. These flow barriers have minor impacts on the advective transport of injected CO_2, because the plume barely touches the fractures as the flow is directed by gravity forces. As a consequence, we observe that differences of residual trapping curves for different inclination angles (shown in Fig. 5d) are insignificant. In post-injection period, such barriers facilitate the dissolution as the CO_2-rich brine tends to propagate alongside these fractures. This phenomenon is clearly depicted in the case with $\theta = 0^\circ$, which has the largest fraction of dissolution trapping after injection ceases - see Fig. 5c.

Next, we place the fracture on the right side near the production well. Time-lapsed behaviors of dissolution and residual trapping are presented in Fig. 9. Variations for different scenarios are unimportant during the injection stage. We observe that the presence of conductive fractures results in a higher residual trapping in the post-injection period - see Fig. 9b. Particularly, the fraction of residual trapping obtained from $\theta = 60^\circ$ deviates from the other two cases as it experiences a relatively steep increase after the dimensionless time $t \approx 4$ (4 times of the injection time period).

To get a better understanding of the underlying physics that govern such process, we look into the related residual (trapped) gas saturation profiles - see Fig. 11. Note that we plot these maps with a saturation range of 0 to 0.27 so as to clearly delineate the distribution of residual gas saturation. Fig. 11 indicates that the majority of trapped gas is gathered beneath the top boundary. In cases of $\theta = 0^\circ$ and 30°, residual saturation maps remain nearly unchanged through the investigated period. However, for $\theta = 60^\circ$, trapped gas becomes visible above the tip of the fracture at $t = 6$. We plot the associated streamline distribution of the liquid phase in this region. As shown, in the case of $\theta = 60^\circ$, the outflow of brine via the fracture invades the zone swept by CO_2, reduces the gas saturation, and eventually leads to an increase in residual

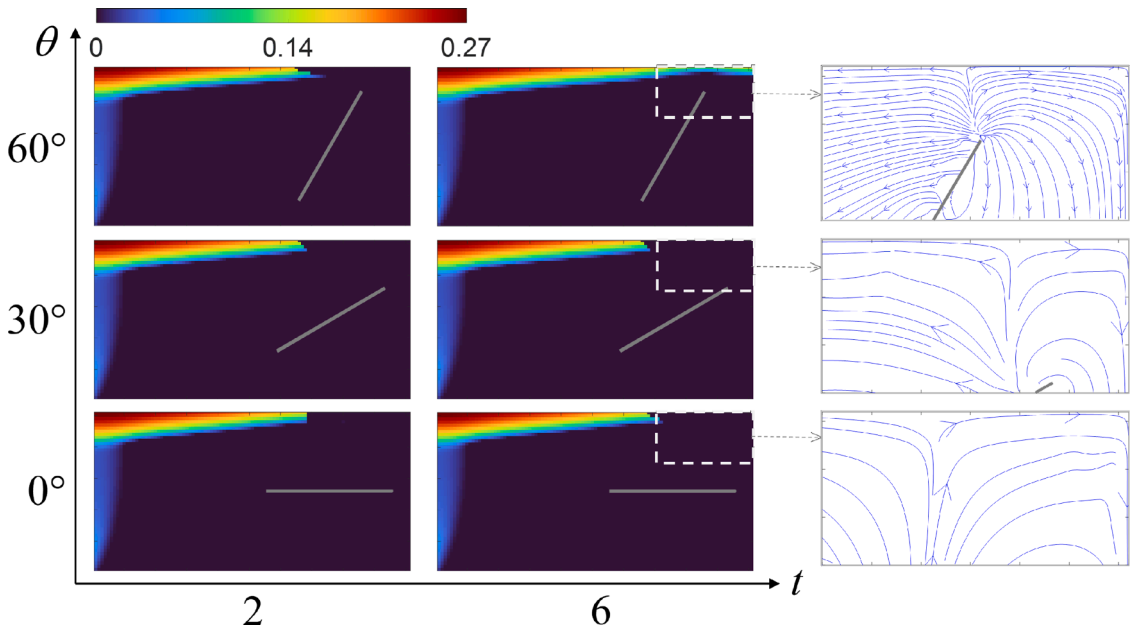

Fig. 11. Residual saturation maps of gas phase in cases of a highly-conductive fracture placed near the production well ($k_m = 8.0 \times 10^{-14}$ m^2). Zoomed-in view of the liquid phase streamline distribution at $t = 6$ is placed next to the associated residual saturation map.

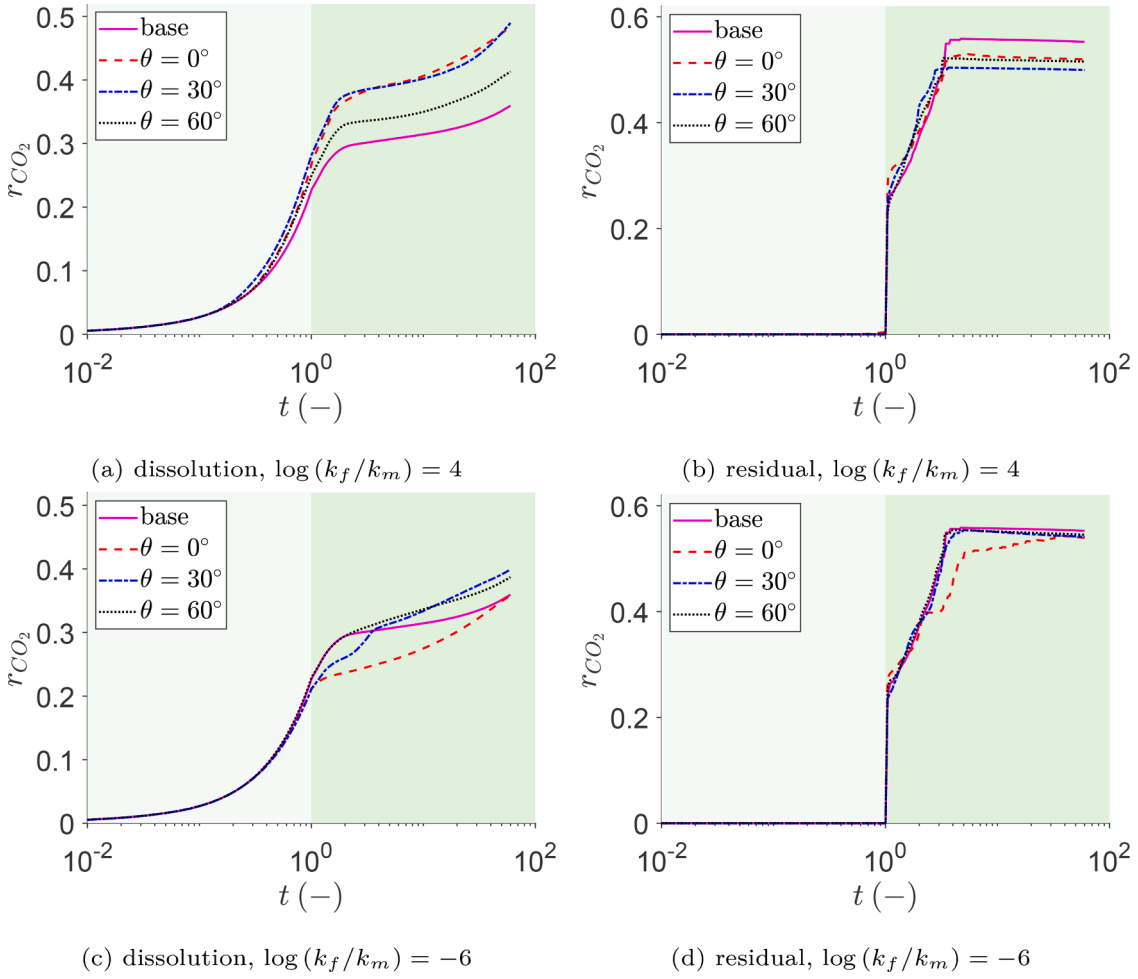

(a) dissolution, $\log(k_f/k_m) = 4$

(b) residual, $\log(k_f/k_m) = 4$

(c) dissolution, $\log(k_f/k_m) = -6$

(d) residual, $\log(k_f/k_m) = -6$

Fig. 12. Fraction of injected CO_2 trapped by different mechanisms in cases of a fracture placing near injection well ($k_m = 4.0 \times 10^{-15}$ m^2).

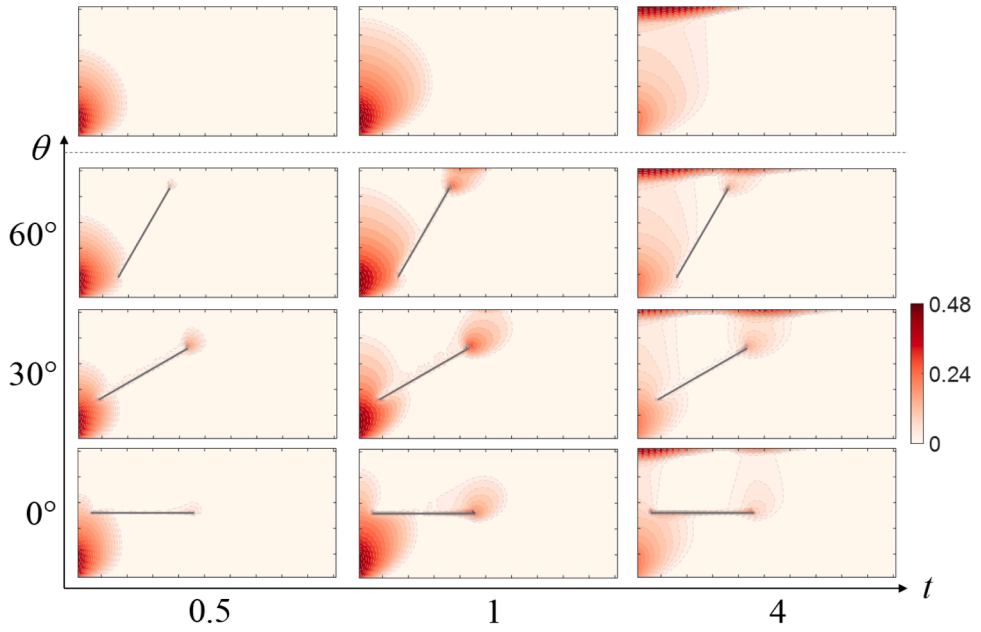

(a) $\log(k_f/k_m) = 4$

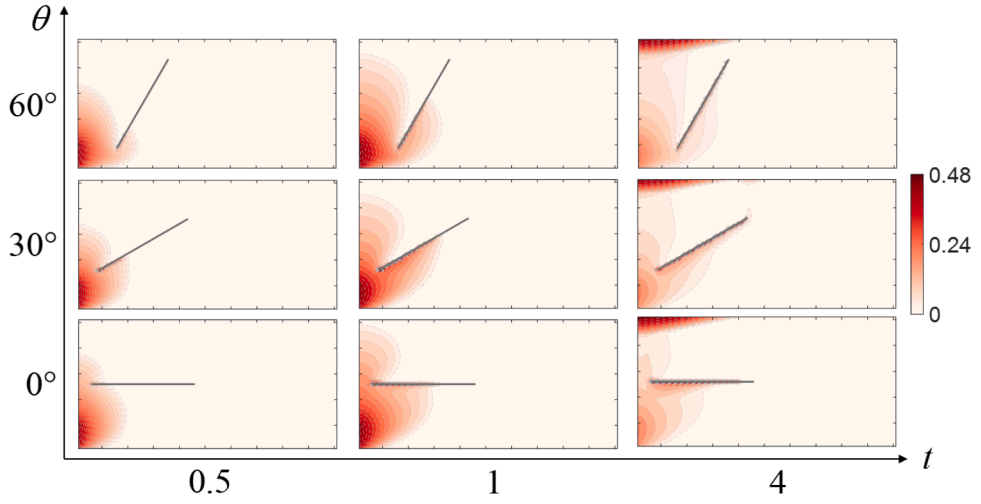

(b) $\log(k_f/k_m) = -6$

Fig. 13. Saturation maps of gas phase in cases of a fracture placed near the injection well ($k_m = 4.0 \times 10^{-15}$ m^2). Results obtained from the base case (without fractures) are presented on top of the cases with $\log(k_f/k_m) = 4$.

trapping. It is worth mentioning that the upward flow of brine is also observed for the other two cases, however, the magnitude of velocity, which is proportional to the density of the streamline, in these two cases is much smaller compared to that of $\theta = 60^\circ$. For this reason the impact of the upward flow on the residual trapping is insignificant.

As for dissolution trapping, the highly conductive fracture cuts both ways. On the one hand, it creates circulation for the liquid phase. This enhances the dissolution by supplying more brine which resides in the bottom toward the upper region of the aquifer. On the other hand, the outflow of brine from the fracture inhibits the generation of descending fingers. As shown in Fig. 10a, none of the investigated cases produce an observable finger on the right side of the aquifer. As a result, fraction curves obtained from $\theta = 0^\circ$ and 30° are quite similar and comparable to that of the base case, whereas for $\theta = 60^\circ$ more CO_2 is dissolved into the brine. This indicates that in this case, the impact of the enhancement of circulation overwhelms that of the inhibition of finger growth in terms of the dissolution trapping. Fig. 10b shows that the flow barriers block the development of falling fingers, which retards the circulation of ambient brine. Such negative feedback is alleviated as θ increases. Since sinking fingers are developed fully at relatively late time of the simulated period, differences of fraction curves are negligible until $t \approx 40$ - see Fig. 9c.

3.2. Single fractured media (low gravity number)

Discussions presented so far consider a relatively high gravity number. In the following subsection we reduce the matrix permeability thereby decreasing the gravity number. Here k_v is reduced from 8.0×10^{-14} m^2 to 4.0×10^{-15} m^2, and N_{gv} becomes $1/20$ of its previous value based on Eq. (2.16). Fig. 13a shows saturation profiles in cases of highly-conductive fractures. Unlike displacements presented in Fig. 6, where injected CO_2 flows quickly to the top, here saturation profiles exhibit a clear lateral migration of CO_2. This is because in low N_{gv} displacements, viscous forces become stronger compared to that in high N_{gv} scenarios; they carry more CO_2 in the horizontal direction. We observe that the fracture intersects the CO_2 plume for all investigated scenarios. In these

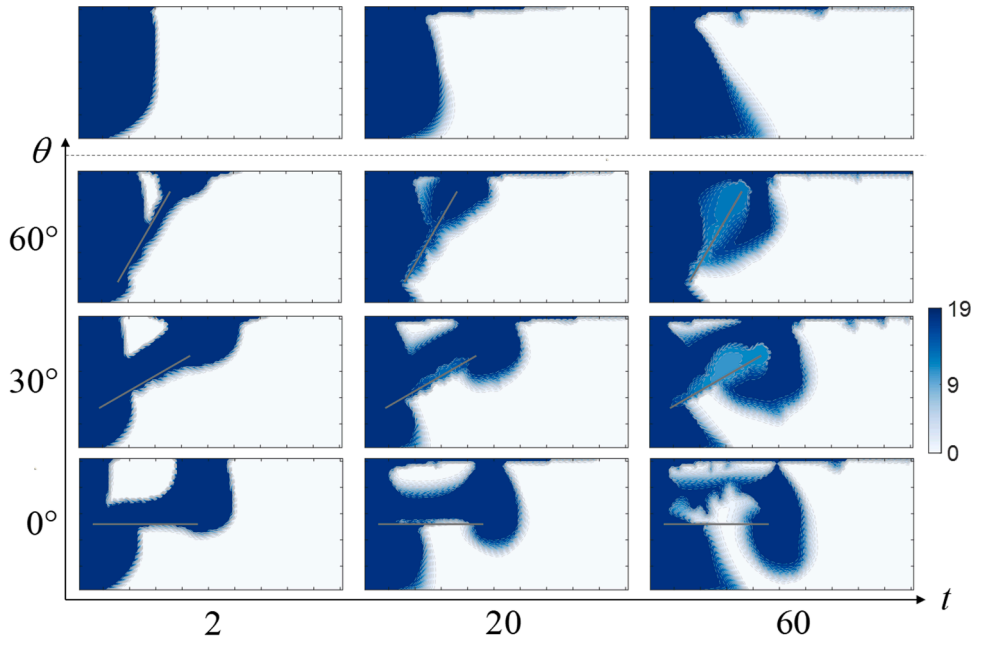

(a) $\log(k_f/k_m) = 4$

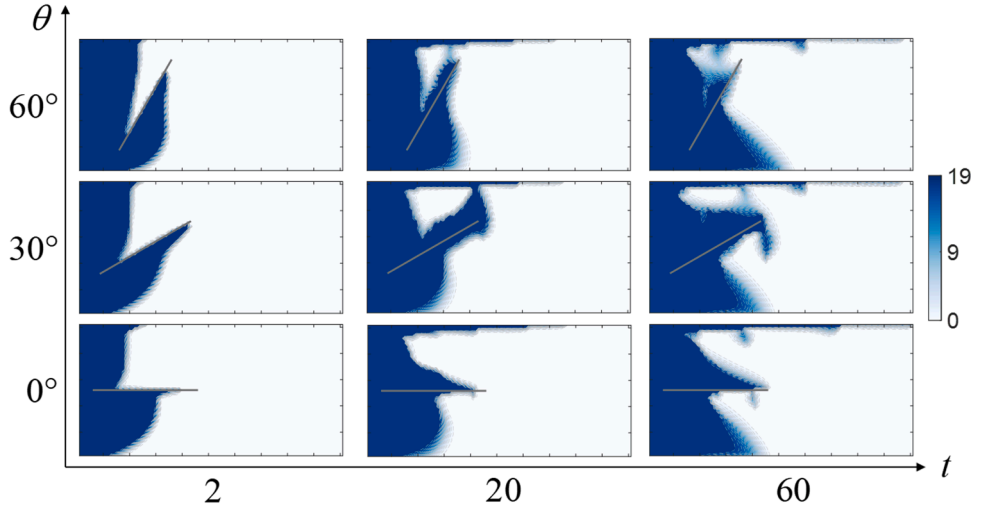

(b) $\log(k_f/k_m) = -6$

Fig. 14. Solution CO_2-brine ratio profiles in cases of a fracture placed near the injection well ($k_m = 4.0 \times 10^{-15}$ m^2). Results obtained from the base case (without fractures) are presented on top of the cases with $\log(k_f/k_m) = 4$.

cases CO_2 prefers flowing through the fracture, and a significant proportion will then migrate upward from the fracture tip.

The fraction of residual trapping in Fig. 12b indicates that compared to high N_{gv} systems, residual trapping occurs over a longer period of time: the curves reach their highest points at later times ($t \approx 4$). Moreover, a smaller amount of CO_2 is trapped in the residual form in the fractured cases. This is to some extent affected by the dissolution which is occurring simultaneously. As shown in Fig. 14a, CO_2 is dissolved along the fracture due to the fact that fractures create additional interfaces between CO_2 and brine: dissolution occurs once the CO_2 leaves the fracture and flows into the matrix. As free CO_2 is being consumed by dissolution, gas phase saturation at the turning point is smaller compared to that for the base case in an average sense. In the post-injection period, highly-conductive fractures induce the circulation shown in Fig. 14a, however, such a circulation does not spread to the entire domain which is otherwise observed in high N_{gv} cases (see Fig. 7a at $t = 60$). Besides, due to the relatively low vertical permeability, the development of sinking fingers is much less active compared to those in cases of $k_m = 8.0 \times 10^{-14}$ m^2.

Saturation maps for the cases of flow barriers are presented in Fig. 13b. Since the barrier impedes the flow, CO_2 plume bifurcates into two branches after intersecting the barrier. The time-lapsed behavior of residual trapping obtained with $\theta = 0^\circ$ deviates from the other cases - see Fig. 12d. To understand this deviation, we take a closer look at the dynamics of plume movement after the cessation of injection. Fig. 15 depicts the evolution of the trailing edge at three moments. The dashed curve represents the contour of the trailing edge, below which the residual trapping occurs. In cases of $\theta = 30^\circ$ and 60°, the CO_2 under the barrier is able to migrate upward along the barrier; however, for a horizontal barrier ($\theta = 0^\circ$), the upward migration of free CO_2 is impeded: CO_2 is accumulated under the barrier. At $t = 3$, we observe that the trailing edge for the cases of $\theta = 30^\circ$ and 60° has risen close to the top boundary. On the other side, free CO_2 is still flowing upward through the opening between the boundary and the barrier in the case of

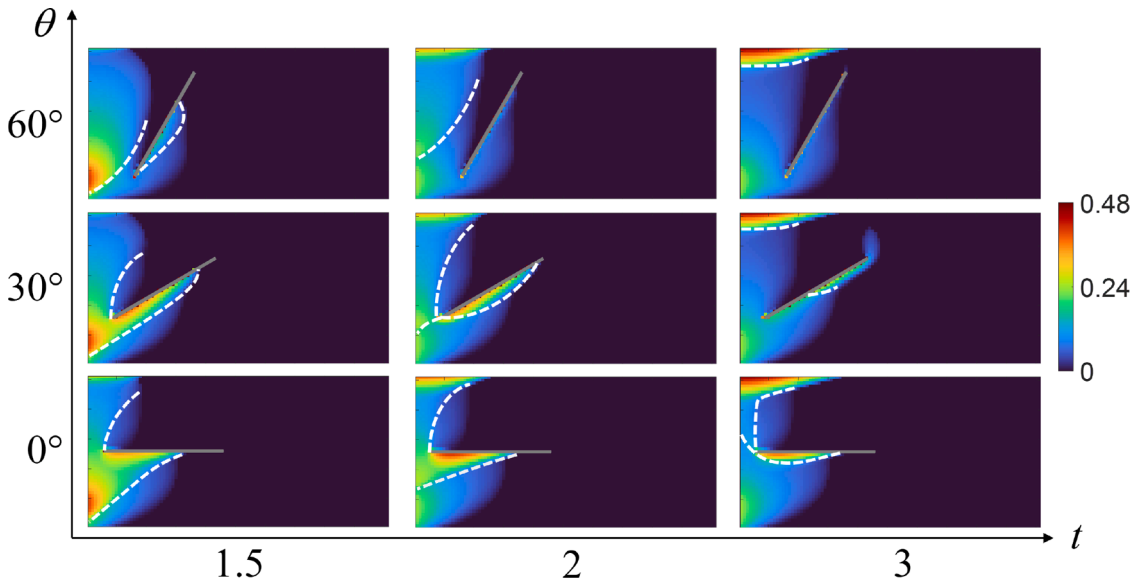

Fig. 15. Evolution of the CO_2 saturation trailing edge (dashed curve) in cases of a flow barrier placed near the injection well ($k_m = 4.0 \times 10^{-15}$ m^2).

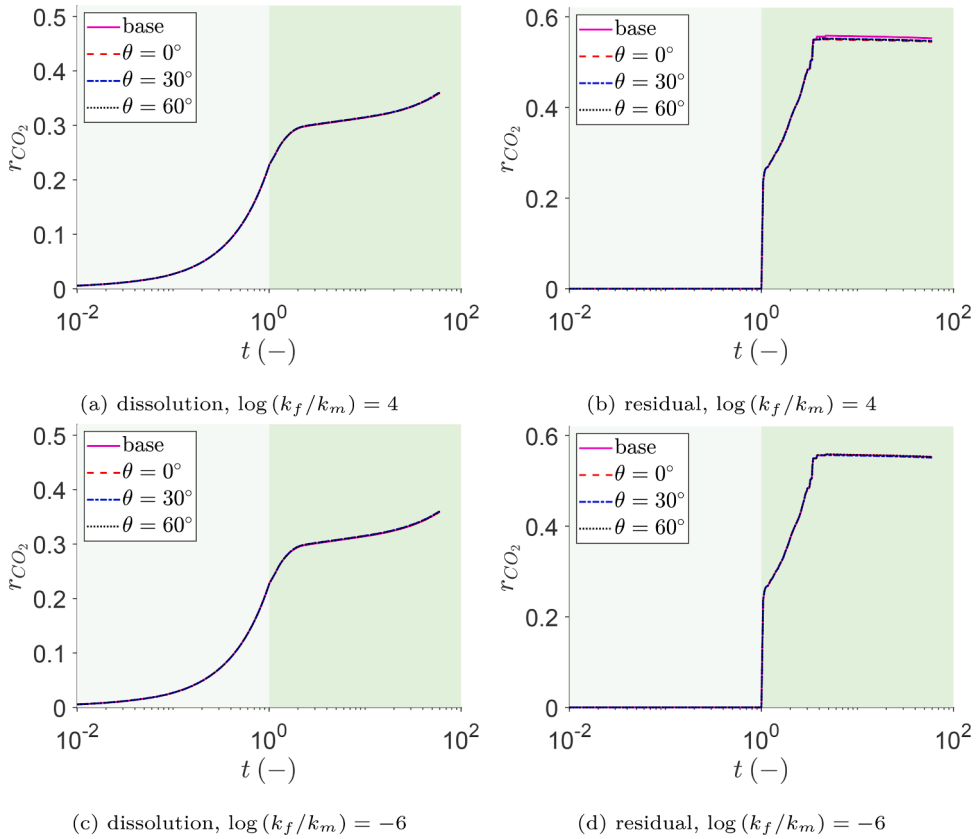

Fig. 16. Fraction of injected CO_2 trapped by different mechanisms in cases of a fracture placed near production well ($k_m = 4.0 \times 10^{-15}$ m^2).

$\theta = 0°$. As a result, the increment of residual trapping is lagging behind. Such movement also retards the dissolution trapping shown in Fig. 12c.

Fraction curves for the fracture placed near the production well are presented in Fig. 16. Since the plume does not migrate far enough to touch the fracture, impacts of fractures, including conductive pathways and flow barriers, on those two trappings are insignificant.

3.3. Fractures with complex geometries

In this subsection we examine how fractures control the dynamics of the trapping process in a complex fracture network representative of a field-scale fracture geometry. The fracture network is generated by the following two steps. First, the seed points denoting the center of individual fracture segments are randomly placed in the model domain. Next, each fracture segment extends from the seed point following the given inclination angle and length. The resulting fracture network used

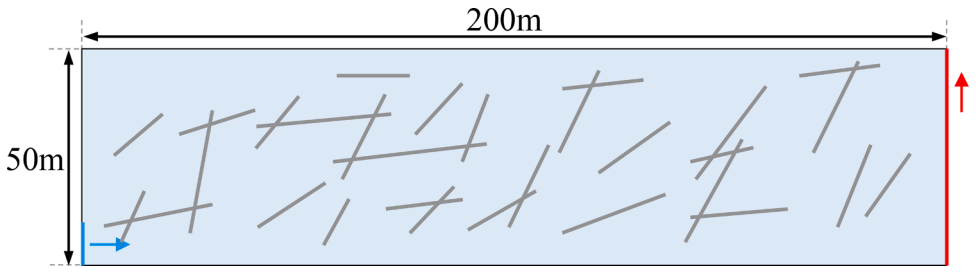

Fig. 17. Schematic of computational domain and fracture geometries for cases of complex fracture network.

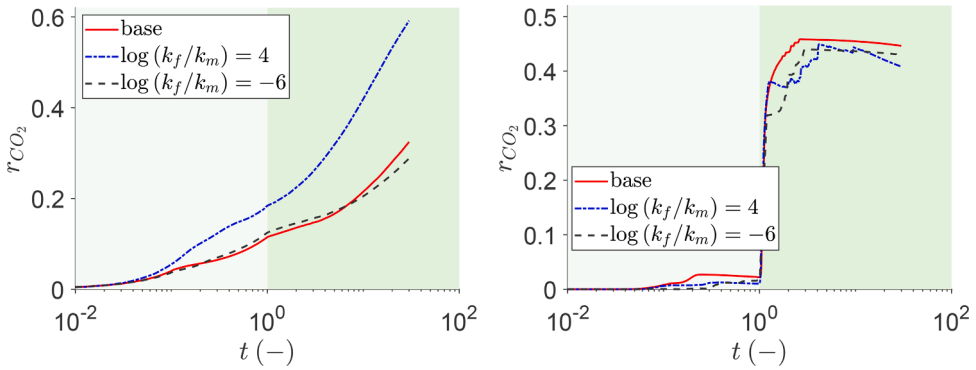

Fig. 18. Fraction of injected CO_2 trapped by different mechanisms in the case of a fracture networks ($k_m = 8.0 \times 10^{-14}$ m^2).

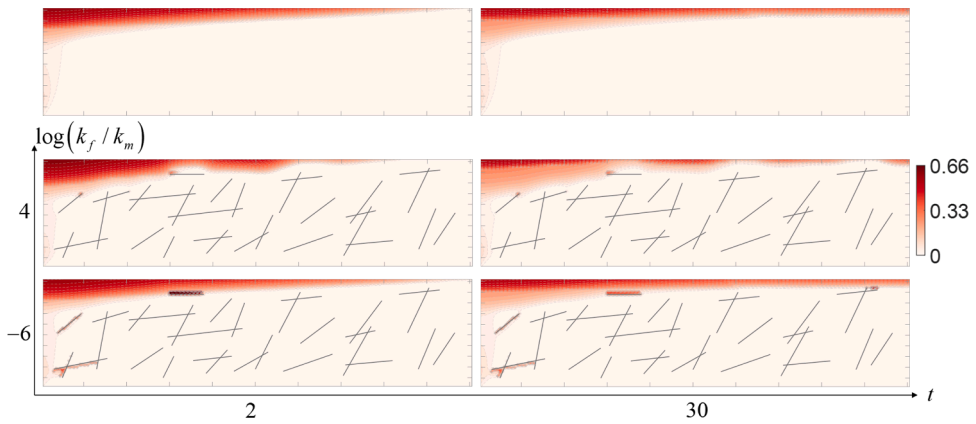

Fig. 19. Saturation maps of gas phase in the case of a fracture network ($k_m = 8.0 \times 10^{-14}$ m^2). Results obtained from the base case (without fractures) are presented on top.

in simulations is depicted in Fig. 17. As shown, the network includes both isolated and intersected fractures.

Fig. 18 presents the temporal evolution of dissolution and residual trapping for $k_m = 8.0 \times 10^{-14}$ m^2. First of all, it is clear that dissolution trapping is enhanced significantly in the case of highly-conductive fractures. The associated solution CO_2-brine ratio profiles at two moments are depicted in Fig. 20. Fractures help the brine to transfer upward, as is observed in previous studies of a single fracture. This is also revealed by saturation maps presented in Fig. 19. In the post-injection period, horizontal migration of gas phase CO_2 underneath the top boundary is interrupted by the upward flow of brine from fracture tips, which leads to a complex dynamic behavior of residual trapping - see Fig. 18b. This movement restricts the gravity-induced convective transport. In the meantime, fresh brine contacts and dissolves CO_2, creating mixing regions in the vicinity of fractures. Note that the upward flow of unsaturated brine also takes place near the bottom boundary - see Fig. 20 at $t = 8$. Such circulation dominates the transport in the post-injection period, and finally, dissolved CO_2 spread across the entire domain.

In addition, Fig. 20 shows that when fractures act as flow barriers, those fractures with low inclination angles near the top boundary play the leading role in impeding the convective transport. As a result, sinking fingers tend to develop through the interval of fracture networks - see Fig. 20 at $t = 30$. Nevertheless, such impediment of flow leads to a smaller dissolution rate compared to that of the base case at late time shown in Fig. 18a.

Simulation results for low N_{gv} cases ($k_m = 4.0 \times 10^{-15}$ m^2) are presented in Fig. 21. Saturation and solution CO_2-brine ratio profiles at two time points, which are identical to those used in high N_{gv} cases, are displayed in Figs. 22 and 23, respectively. Fig. 22 shows that due to relatively strong viscous forces, a larger portion of injected CO_2 flows in the lateral direction, and interacts with fractures near the injection well:

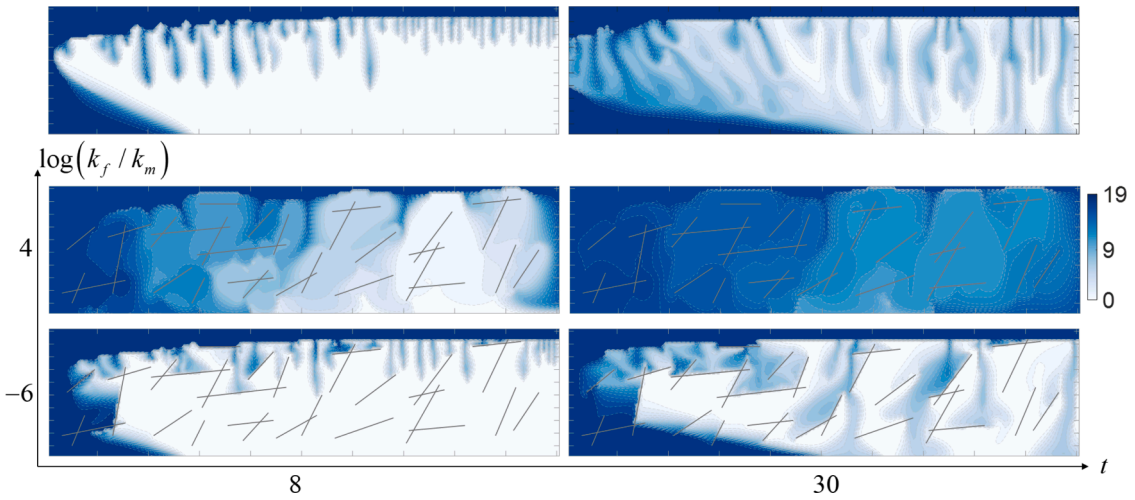

Fig. 20. Solution CO_2-brine ratio profiles in case of fracture network ($k_m = 8.0 \times 10^{-14}$ m^2). Results obtained from the base case (without fractures) are presented on top.

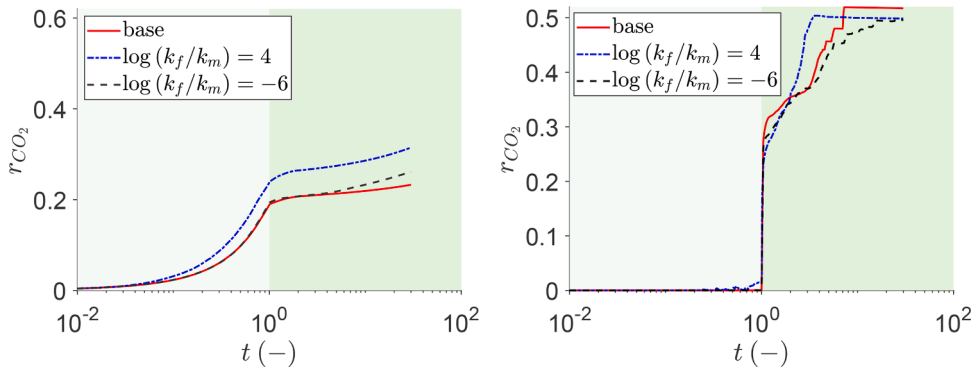

Fig. 21. Fraction of injected CO_2 trapped by different mechanisms in the case of a fracture network ($k_m = 4.0 \times 10^{-15}$ m^2).

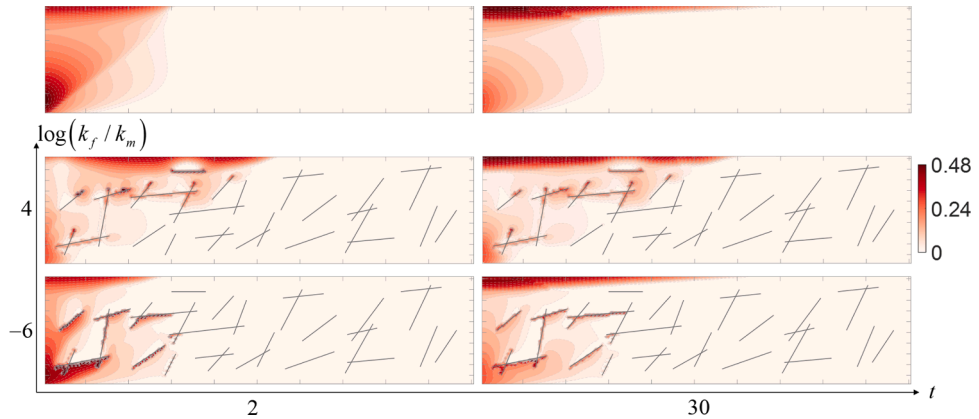

Fig. 22. Saturation maps of gas phase in the case of a fracture network ($k_m = 4.0 \times 10^{-15}$ m^2). Results obtained from the base case (without fractures) are presented on top.

in case of flow barriers, CO_2 migrates underneath the barriers with low inclination angles; for conductive fractures, CO_2 flows through the fracture network and escapes from fracture tips. These interactions create tortuous interfaces which are beneficial for dissolution trapping.

Solution CO_2-brine ratio profiles obtained from the base case indicate that the gravity-induced convective transport is limited in the post-injection period. It is expected that presence of highly conductive fractures promotes fluid mixing, as shown in Fig. 23. An interesting fact is that the fraction of dissolved CO_2 obtained from the case of $\log(k_f/k_m) = -6$ is higher than that of the base case at late time. This is also observed in the study of a single fracture. Flow barriers with low inclination angles are favorable for the dissolution process: saturated brine would propagate along such inner boundaries created by flow barriers. However, fractures with large inclination angles are

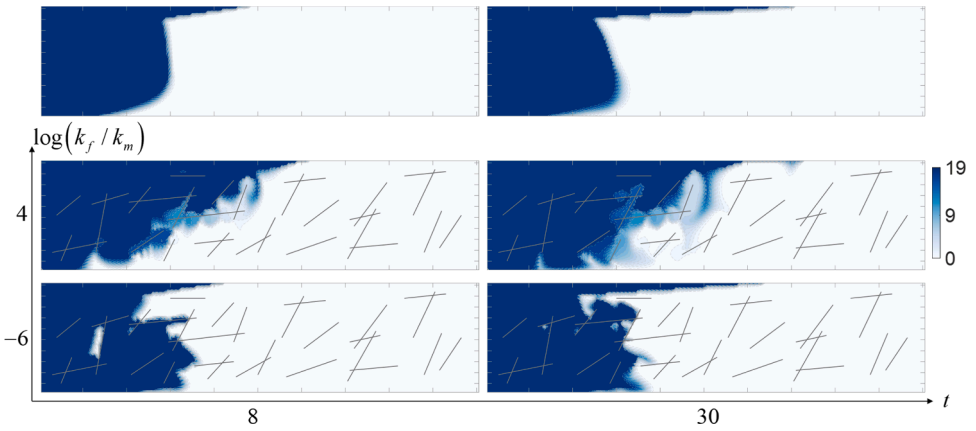

Fig. 23. Solution CO_2-brine ratio profiles in the case of a fracture network ($k_m = 4.0 \times 10^{-15}$ m^2). Results obtained from the base case (without fractures) are presented on top.

disadvantageous for dissolution trapping because they block such propagation shown in Fig. 23.

4. Conclusions

In this work, we investigate the role of fractures on CO_2 storage in a full cycle process, including injection, migration and post-migration periods. The projection-based discrete fracture model is employed to model fractures with varying conductivities. Essential trapping mechanisms in hydrodynamic trapping, i.e., residual and dissolution ones, are accounted for and incorporated in a unified framework based on the compositional formulation. The developed simulator is first applied to a synthetic domain with a single fracture. The interplay of driving forces, i.e., viscous and gravity forces are studied by varying absolute permeability of the matrix. In each scenario, simulations are conducted for cases consisting of different fracture geometries and permeability. The temporal evolution of trapped amount due to residual and dissolution trapping is quantified.

Results indicate that in the case of a high gravity number, conductive fractures in general enhance fluid mixing between two phases via the upward flow of brine. Such enhancement becomes more pronounced for fractures with a higher inclination angle, and it affects residual trapping if the outflow of brine meets the gas phase CO_2 migrating along the top boundary. As for flow barriers, their geometry has little impact on residual trapping because the flow is controlled by gravity forces. On the other hand, the dissolution process is influenced by the geometry of flow barriers: the fracture could either benefit the dissolution by creating additional inner boundaries or weaken fluid mixing by blocking the convective transport.

In the case of a low gravity number, the impact of fractures on the trapping behavior depends on fracture positions to a great extent. In this scenario viscous forces become more prominent such that fluid movement is more active in the horizontal direction. Fractures placed near the injection well have a better chance to interfere with the displacement process. And consequently, different inclination angles result in differing dynamics for both residual and dissolution trapping processes.

We then apply the model to a larger-domain with a complex fracture network generated based on a statistical approach. We find that the fluid dynamics and the associated trapping processes observed in simple fracture geometry also appear in the larger-domain with complex fracture network. Compared to the base case without fractures, the presence of a conductive-fracture network facilitates dissolution trapping while undermining residual trapping. Moreover, a flow barrier network benefits dissolution trapping in systems of a relatively low gravity number.

The present work provides a comprehensive understanding of the role of fractures with varying fracture-matrix permeability ratios in a full-cycle of CO_2 storage in saline aquifers. We emphasize that the accurate characterization of fracture geometry and its conductivity is essential for evaluation of the trapped CO_2 amount. This study is performed based on a two-dimensional model and fractures are represented by lower-dimensional line segments. A possible direction for future work is to extend the current model to be fully three-dimension. This would afford the capability to assess CO_2 storage in more practical applications.

CRediT authorship contribution statement

Yuhang Wang: Conceptualization, Methodology, Software, Formal analysis, Writing – original draft. **Cornelis Vuik:** Methodology, Writing – review & editing, Supervision. **Hadi Hajibeygi:** Conceptualization, Methodology, Writing – review & editing, Supervision, Funding acquisition.

Declaration of Competing Interest

The authors declare that they have no known competing financial interests or personal relationships that could have appeared to influence the work reported in this paper.

Acknowledgment

Hadi Hajibeygi was sponsored by the Dutch National Science Foundation (NWO) under Vidi Project “ADMIRE” (project number 17509). We thank the ADMIRE user committee for allowing us to publish this paper. Group members of DARSim (Delft Advanced Reservoir Simulation) and ADMIRE (Adaptive Dynamic Multiscale Integrated Reservoir Earth) are acknowledged for fruitful discussions during the development of this work. The source code developed for this research is openly accessible via https://gitlab.com/darsim address.

References

Ahmed, R., Edwards, M.G., Lamine, S., Huisman, B.A.H., Pal, M., 2015. Control-volume distributed multi-point flux approximation coupled with a lower-dimensional fracture model. J. Comput. Phys. 284, 462–489.
Ahmed, R., Li, J., 2019. A numerical framework for two-phase flow of CO_2 injection into fractured water-saturated reservoirs. Adv. Water Resour. 130, 283–299.
Aziz, K., 1979. Petroleum Reservoir Simulation, vol. 476. Applied Science Publishers.
Bachu, S., 2002. Sequestration of CO_2 in geological media in response to climate change: road map for site selection using the transform of the geological space into the CO_2 phase space. Energy Convers. Manage. 43 (1), 87–102.
Bachu, S., Gunter, W.D., Perkins, E.H., 1994. Aquifer disposal of CO_2: hydrodynamic and mineral trapping. Energy Convers. Manage. 35 (4), 269–279.
Benson, S.M., Cole, D.R., 2008. CO_2 Sequestration in deep sedimentary formations. Elements 4 (5), 325–331.
Berkowitz, B., 2002. Characterizing flow and transport in fractured geological media: a review. Adv. Water Resour. 25 (8–12), 861–884.

Berre, I., Boon, W.M., Flemisch, B., Fumagalli, A., Gläser, D., Keilegavlen, E., Scotti, A., Stefansson, I., Tatomir, A., Brenner, K., et al., 2021. Verification benchmarks for single-phase flow in three-dimensional fractured porous media. Adv. Water Resour. 147, 103759.
Berre, I., Doster, F., Keilegavlen, E., 2019. Flow in fractured porous media: a review of conceptual models and discretization approaches. Transp. Porous Media 130 (1), 215–236.
Bruant, R., Guswa, A., Celia, M., Peters, C., 2002. Safe storage of CO_2 in deep saline aquifers. Environ. Sci. Technol. 36 (11), 240A–245A.
Carlson, F.M., 1981. Simulation of relative permeability hysteresis to the nonwetting phase. SPE Annual Technical Conference and Exhibition. Society of Petroleum Engineers.
Ţene, M., Al Kobaisi, M.S., Hajibeygi, H., 2016. Algebraic multiscale method for flow in heterogeneous porous media with embedded discrete fractures (f-AMS). J. Comput. Phys. 321, 819–845.
Ţene, M., Bosma, S.B.M., Al Kobaisi, M.S., Hajibeygi, H., 2017. Projection-based embedded discrete fracture model (pEDFM). Adv. Water Resour. 105, 205–216.
Cusini, M., Fryer, B., van Kruijsdijk, C., Hajibeygi, H., 2018. Algebraic dynamic multilevel method for compositional flow in heterogeneous porous media. J. Comput. Phys. 354, 593–612.
Dai, Z., Xu, L., Xiao, T., McPherson, B., Zhang, X., Zheng, L., Dong, S., Yang, Z., Soltanian, M.R., Yang, C., et al., 2020. Reactive chemical transport simulations of geologic carbon sequestration: methods and applications. Earth Sci. Rev. 103265.
Dockrill, B., Shipton, Z.K., 2010. Structural controls on leakage from a natural CO_2 geologic storage site: Central Utah, USA. J. Struct. Geol. 32 (11), 1768–1782.
Eiken, O., Ringrose, P., Hermanrud, C., Nazarian, B., Torp, T.A., Høier, L., 2011. Lessons learned from 14 years of CCS operations: Sleipner, In Salah and Snøhvit. Energy Procedia 4, 5541–5548.
Emami-Meybodi, H., Hassanzadeh, H., Green, C.P., Ennis-King, J., 2015. Convective dissolution of CO_2 in saline aquifers: progress in modeling and experiments. Int. J. Greenhouse Gas Control 40, 238–266.
Espinoza, D.N., Santamarina, J.C., 2017. CO_2 Breakthrough-Caprock sealing efficiency and integrity for carbon geological storage. Int. J. Greenhouse Gas Control 66, 218–229.
Fanchi, J.R., 2005. Principles of Applied Reservoir Simulation. Elsevier.
Flemisch, B., Berre, I., Boon, W., Fumagalli, A., Schwenck, N., Scotti, A., Stefansson, I., Tatomir, A., 2018. Benchmarks for single-phase flow in fractured porous media. Adv. Water Resour. 111, 239–258.
Flemisch, B., Fumagalli, A., Scotti, A., 2016. A review of the XFEM-based approximation of flow in fractured porous media. Adv. Discretization Methods 47–76.
Fumagalli, A., Pasquale, L., Zonca, S., Micheletti, S., 2016. An upscaling procedure for fractured reservoirs with embedded grids. Water Resour. Res. 52 (8), 6506–6525.
Fumagalli, A., Zonca, S., Formaggia, L., 2017. Advances in computation of local problems for a flow-based upscaling in fractured reservoirs. Math. Comput. Simul. 137, 299–324.
Gunter, W.D., Perkins, E.H., Hutcheon, I., 2000. Aquifer disposal of acid gases: modelling of water–rock reactions for trapping of acid wastes. Appl. Geochem. 15 (8), 1085–1095.
Hajibeygi, H., Karvounis, D., Jenny, P., 2011. A hierarchical fracture model for the iterative multiscale finite volume method. J. Comput. Phys. 230 (24), 8729–8743.
Hassanzadeh, H., Pooladi-Darvish, M., Elsharkawy, A.M., Keith, D.W., Leonenko, Y., 2008. Predicting PVT data for CO_2–brine mixtures for black-oil simulation of CO_2geological storage. Int. J. Greenhouse Gas Control 2 (1), 65–77.
HosseiniMehr, M., Cusini, M., Vuik, C., Hajibeygi, H., 2018. Algebraic dynamic multilevel method for embedded discrete fracture model (F-ADM). J. Comput. Phys. 373, 324–345.
Hui, M.-H.R., Karimi-Fard, M., Mallison, B., Durlofsky, L.J., 2018. A general modeling framework for simulating complex recovery processes in fractured reservoirs at different resolutions. SPE J. 23 (02), 598–613.
Ide, S.T., Jessen, K., Orr Jr., F.M., 2007. Storage of CO_2 in saline aquifers: effects of gravity, viscous, and capillary forces on amount and timing of trapping. Int. J. Greenhouse Gas Control 1 (4), 481–491.
Iding, M., Ringrose, P., 2010. Evaluating the impact of fractures on the performance of the in salah CO_2 storage site. Int. J. Greenhouse Gas Control 4 (2), 242–248.
Jiang, J., Younis, R.M., 2015. Numerical study of complex fracture geometries for unconventional gas reservoirs using a discrete fracture-matrix model. J. Nat. Gas Sci. Eng. 26, 1174–1186.
Joekar-Niasar, V., Doster, F., Armstrong, R.T., Wildenschild, D., Celia, M.A., 2013. Trapping and hysteresis in two-phase flow in porous media: a pore-network study. Water Resour. Res. 49 (7), 4244–4256.
Juanes, R., Spiteri, E.J., Orr Jr., F.M., Blunt, M.J., 2006. Impact of relative permeability hysteresis on geological CO_2 storage. Water Resour. Res. 42 (12).
Karimi-Fard, M., Durlofsky, L.J., 2016. A general gridding, discretization, and coarsening methodology for modeling flow in porous formations with discrete geological features. Adv. Water Resour. 96, 354–372.
Karimi-Fard, M., Durlofsky, L.J., Aziz, K., 2004. An efficient discrete-fracture model applicable for general-purpose reservoir simulators. SPE J. 9 (02), 227–236.
Killough, J.E., 1976. Reservoir simulation with history-dependent saturation functions. Soc. Pet. Eng. J. 16 (01), 37–48.
Kim, K.-Y., Oh, J., Han, W.S., Park, K.G., Shinn, Y.J., Park, E., 2018. Two-phase flow visualization under reservoir conditions for highly heterogeneous conglomerate rock: a core-scale study for geologic carbon storage. Sci. Rep. 8 (1), 1–10.
Kim, M., Kim, K.-Y., Han, W.S., Oh, J., Park, E., 2019. Density-driven convection in a fractured porous media: implications for geological CO_2 storage. Water Resour. Res. 55 (7), 5852–5870.
Lee, S.H., Jensen, C.L., Lough, M.F., 2000. Efficient finite-difference model for flow in a reservoir with multiple length-scale fractures. SPE J. 5 (03), 268–275.
Li, L., Lee, S.H., 2008. Efficient field-scale simulation of black oil in a naturally fractured reservoir through discrete fracture networks and homogenized media. SPE Reservoir Eval. Eng. 11 (04), 750–758.
Lucier, A., Zoback, M., 2008. Assessing the economic feasibility of regional deep saline aquifer CO_2 injection and storage: ageomechanics-based workflow applied to the Rose Run sandstone in Eastern Ohio, USA. Int. J. Greenhouse Gas Control 2 (2), 230–247.
Moës, N., Dolbow, J., Belytschko, T., 1999. A finite element method for crack growth without remeshing. Int. J. Numer. Methods Eng. 46 (1), 131–150.
Moinfar, A., Varavei, A., Sepehrnoori, K., Johns, R.T., 2014. Development of an efficient embedded discrete fracture model for 3D compositional reservoir simulation in fractured reservoirs. SPE J. 19 (02), 289–303.
Mustapha, H., Dimitrakopoulos, R., Graf, T., Firoozabadi, A., 2011. An efficient method for discretizing 3D fractured media for subsurface flow and transport simulations. Int. J. Numer. Methods Fluids 67 (5), 651–670.
Neufeld, J.A., Hesse, M.A., Riaz, A., Hallworth, M.A., Tchelepi, H.A., Huppert, H.E., 2010. Convective dissolution of carbon dioxide in saline aquifers. Geophys. Res. Lett. 37 (22).
Ni, H., Boon, M., Garing, C., Benson, S.M., 2019. Predicting CO_2 residual trapping ability based on experimental petrophysical properties for different sandstone types. Int. J. Greenhouse Gas Control 86, 158–176.
Norbeck, J.H., McClure, M.W., Lo, J.W., Horne, R.N., 2016. An embedded fracture modeling framework for simulation of hydraulic fracturing and shear stimulation. Comput. Geosci. 20 (1), 1–18.
Oak, M.J., Baker, L.E., Thomas, D.C., 1990. Three-phase relative permeability of Berea sandstone. J. Pet. Technol. 42 (08), 1–054.
Plohr, B., Marchesin, D., Bedrikovetsky, P., Krause, P., 2001. Modeling hysteresis in porous media flow via relaxation. Comput. Geosci. 5 (3), 225–256.
Raziperchikolaee, S., Alvarado, V., Yin, S., 2013. Effect of hydraulic fracturing on long-term storage of CO_2 in stimulated saline aquifers. Appl. Energy 102, 1091–1104.
Reichenberger, V., Jakobs, H., Bastian, P., Helmig, R., 2006. A mixed-dimensional finite volume method for two-phase flow in fractured porous media. Adv. Water Resour. 29 (7), 1020–1036.
Ren, F., Ma, G., Wang, Y., Fan, L., Zhu, H., 2017. Two-phase flow pipe network method for simulation of CO_2 sequestration in fractured saline aquifers. Int. J. Rock Mech. Min. Sci. 98, 39–53.
Rinaldi, A.P., Rutqvist, J., Cappa, F., 2014. Geomechanical effects on CO_2leakage through fault zones during large-scale underground injection. Int. J. Greenhouse Gas Control 20, 117–131.
Ruprecht, C., Pini, R., Falta, R., Benson, S., Murdoch, L., 2014. Hysteretic trapping and relative permeability of CO_2 in sandstone at reservoir conditions. Int. J. Greenhouse Gas Control 27, 15–27.
Rutqvist, J., 2012. The geomechanics of CO_2 storage in deep sedimentary formations. Geotech. Geol. Eng. 30 (3), 525–551.
Shafabakhsh, P., Ataie-Ashtiani, B., Simmons, C.T., Younes, A., Fahs, M., 2021. Convective-reactive transport of dissolved CO_2 in fractured-geological formations. Int. J. Greenhouse Gas Control 109, 103365.
Soltanian, M.R., Amooie, M.A., Dai, Z., Cole, D., Moortgat, J., 2016. Critical dynamics of gravito-convective mixing in geological carbon sequestration. Sci. Rep. 6 (1), 1–13.
Spycher, N., Pruess, K., Ennis-King, J., 2003. CO_2–H_2O mixtures in the geological sequestration of CO_2. I. Assessment and calculation of mutual solubilities from 12 to 100 °c and up to 600 bar. Geochim. Cosmochim. Acta 67 (16), 3015–3031.
Steffy, D.A., Barry, D.A., Johnston, C.D., 1997. Influence of antecedent moisture content on residual LNAPL saturation. Soil Sediment Contam. 6 (2), 113–147.
Sun, J., Gamboa, E.S., Schechter, D., Rui, Z., 2016. An integrated workflow for characterization and simulation of complex fracture networks utilizing microseismic and horizontal core data. J. Nat. Gas Sci. Eng. 34, 1347–1360.
van Genuchten, M.T., 1980. A closed-form equation for predicting the hydraulic conductivity of unsaturated soils. Soil Sci. Soc. Am. J. 44 (5), 892–898.
Voskov, D.V., Tchelepi, H.A., 2012. Comparison of nonlinear formulations for two-phase multi-component EoS based simulation. J. Pet. Sci. Eng. 82, 101–111.
Wang, Y., Shahvali, M., 2016. Discrete fracture modeling using Centroidal Voronoi grid for simulation of shale gas plays with coupled nonlinear physics. Fuel 163, 65–73.
Wang, Y., Vuik, C., Hajibeygi, H., 2022. Analysis of hydrodynamic trapping interactions during full-cycle injection and migration of CO_2 in deep saline aquifers. Adv. Water Resour. 159, 104073.
Xu, F., Hajibeygi, H., Sluys, L.J., 2021. Multiscale extended finite element method for deformable fractured porous media. J. Comput. Phys. 436, 110287.
Xu, Y., Cavalcante Filho, J.S., Yu, W., Sepehrnoori, K., 2017. Discrete-fracture modeling of complex hydraulic-fracture geometries in reservoir simulators. SPE Reservoir Eval. Eng. 20 (02), 403–422.
Zappone, A., Rinaldi, A.P., Grab, M., Wenning, Q.C., Roques, C., Madonna, C., Obermann, A.C., Bernasconi, S.M., Brennwald, M.S., Kipfer, R., et al., 2021. Fault sealing and caprock integrity for CO_2 storage: an in situ injection experiment. Solid Earth 12 (2), 319–343.
Zhang, L., Zhang, S., Jiang, W., Wang, Z., Li, J., Bian, Y., 2018. A mechanism of fluid exchange associated to CO_2 leakage along activated fault during geologic storage. Energy 165, 1178–1190.